Anatomy of an Alpine bedload transport event: a watershed-scale seismic-network perspective

Gilles Antoniazza[1,2], Michael Dietze[3,4], Davide Mancini[1], Jens M. Turowski[3], Dieter Rickenmann[2], Tobias Nicollier[2], Stefan Boss[2] and Stuart N. Lane[1]

[1]University of Lausanne, Institute of Earth Surface Dynamics (IDYST), Lausanne, Switzerland.

[2]Swiss Federal Research Institute WSL, Mountain Hydrology and Mass Movements, Birmensdorf, Switzerland.

[3]German Research Center for Geosciences (GFZ), Section 4.6 Geomorphology, Potsdam, Germany.

[4]Georg-August University Göttingen, Faculty of Geosciences and Geography, Göttingen, Germany.

Abstract

The way Alpine rivers mobilize, convey and store coarse material during high-magnitude events is poorly understood, notably because it is difficult to obtain measurements of bedload transport at the watershed scale. Seismic sensor data, evaluated with appropriate seismic physical models, can provide that missing link by yielding absolute time-series of bedload transport. Low cost and ease of installation allows for networks of sensors to be deployed, providing continuous, watershed-scale insights into bedload transport dynamics. Here, we deploy a network of 24 seismic sensors to capture the motion of coarse material in a 13.4 km^2 Alpine watershed during a high-magnitude bedload transport event. First, we benchmark the seismic inversion routine with an independent time-series obtained with a calibrated acoustic system. Then, we apply the procedure to the other seismic sensors across the watershed. Spatially-distributed time-series of bedload transport reveal a relative inefficiency of Alpine watersheds in evacuating coarse material, even during a relatively infrequent high-magnitude bedload transport event. Significant inputs measured for some tributaries were rapidly attenuated as the main river crossed less hydraulically-efficient reaches, and only a comparatively negligible proportion of the total amount of material mobilized in the watershed was exported at the outlet. Cross-correlation analysis of the time-series suggests that a faster moving water wave (re-)mobilizes local material and bedload is expected to move slower, and over shorter distances. Multiple periods of competent flows are likely to be necessary to evacuate the coarse material produced throughout the watershed during individual source-mobilizing bedload transport events.

Plain Language Summary

By driving erosion and deposition, bedload transport is a serious challenge for Alpine watershed management. Yet, the way Alpine rivers mobilize, convey and store coarse material during high-magnitude events is poorly constrained, notably due to the difficulty of measuring bedload transport at the watershed scale.

In this contribution, we use a network of 24 seismic sensors to capture the motion of coarse material in the 13.4 km^2 Vallon de Nant Alpine watershed during a high-magnitude bedload transport event. Spatially-distributed absolute time-series of bedload transport reveal a relative inefficiency of Alpine watersheds in evacuating coarse material, even during a relatively high-magnitude bedload transport event. Large inputs measured in some tributaries are indeed rapidly attenuated as the flow crosses less hydraulically-efficient reaches, and only a comparatively negligible proportion of the total amount of material mobilized in the watershed is exported at the outlet. Coarse material is expected to move slowly, and over relatively short distances. This dataset increases knowledge of coarse material motion within Alpine watersheds during high-magnitude bedload transport events, and may help improve predictions of bedload transport in the future through a better constraint on changes in sediment availability in space and time.

Key points:

- For the first time, a high-magnitude bedload transport event is captured at the watershed scale by a network of 24 seismic sensors.
- A comparatively low proportion of the material mobilized in the watershed during the event is exported at the outlet (2.5 %).
- Multiple periods of competent flows are necessary to evacuate coarse material produced during individual source-mobilizing events.

Key-words: Bedload transport, environmental seismology, Swiss Plate Geophone system (SPG), coarse material flux, Alpine watershed.

1. Introduction

Bedload transport is an important component of watershed management within Alpine areas, through its conditioning of river morphology, the benefit it delivers to riverine ecosystems, and its important contribution to sediment budgets of lowland fluvial systems (Wohl, 2006, 2013; Badoux et al., 2014, 2016). Yet, the way Alpine watersheds produce, convey and store coarse material is still poorly understood (Cavalli et al., 2013; Dell'Agnese et al., 2015; Lane et al., 2017; Comiti et al., 2019). This represents a major limit to the usefulness of current bedload transport equations, since knowledge of change in sediment availability through time and space is needed for improving bedload transport predictions of Alpine rivers (Piton and Recking, 2017; Gomez and Soar, 2022).

The morphology of Alpine rivers largely derives from their glacier legacy, with a typical long-profile comprising a succession of steep rockwalls and hillslopes, flatter and wider glacier troughs, and steeper glacier riegls (Hooke, 1991; Cook and Swift, 2012; Egholm et al., 2012; Antoniazza and Lane, 2021). Alpine rivers tend to develop different morphologies along sections that present contrasting topographic and hydraulic properties. In the flatter sections, usually covered by Quaternary material, the river is typically alluvial with plane-bed or braided morphologies (Piton and Recking, 2017; Mao et al., 2017; Lane et al., 2017;

Comiti et al., 2019). In the steeper and sometimes more confined sections, semi-alluvial reaches tend to develop cascades or step-pool morphologies (Recking et al., 2012; Turowski, 2012; Yager et al., 2012). The streambed is made of a mixture of alluvial deposits and immobile or poorly-mobile larger particles issuing from hillslope processes (e.g. landslides, debris flow), from deglaciation deposits, or from bedrock outcrops. Along these reaches, the streambed is typically armored, resulting in limited sediment availability (Turowski et al., 2009; Recking et al., 2012; Yager et al., 2012; Piton and Recking, 2017). Alpine rivers are also often colluvial in their headwater reaches, which means that there may be intermittent material supply from tributaries (Piton and Recking, 2017; Rainato et al., 2017).

The efficiency with which bedload is mobilized, transported and deposited may vary between these different morphological sections (Dell'Agnese et al., 2015; Lane et al., 2017; Comiti et al., 2019). Alluvial reaches may alternatively act as sediment sources or sinks, but may not always be hydraulically efficient in conveying coarse material (Dell'Agnese et al., 2015; Lane et al., 2017; Mao et al., 2017). Semi-alluvial reaches are steeper, but also rougher, and evidence suggests that bedload may 'travel' without major reworking of the underlying streambed along those sections (Mueller and Pitlick, 2005; Recking et al., 2012; Piton and Recking, 2017). In colluvial systems, tributaries may supply material into the main channel, as long as their (diffusive) alluvial fans are not disconnecting the main river from the steep gullies draining the hillslopes (Lane et al., 2017; Rainato et al., 2017; Mancini and Lane, 2020). In this context, multiple studies have advocated a relative inefficiency of Alpine watersheds in conveying coarse material (Cavalli et al., 2013; Dell'Agnese et al., 2015; Lane et al., 2017). Despite questioning of the ability of high-magnitude flow events to increase hillslope coupling and to permit the efficient transfer of large amount of bedload through various morphological reaches of Alpine watersheds (Cavalli et al., 2013; Dell'Agnese et al., 2015; Lane et al., 2017; Rainato et al., 2017, 2018), this premise has been rarely tested with field data.

A primary reason for the lacking empirical support of limited export efficiency is the difficulty of monitoring bulk bedload transport throughout Alpine watersheds. Particle tracking experiments have provided insights into the motion of individual particles across different morphological sections of Alpine watersheds (Schneider et al., 2014; Dell'Agnese et al., 2015; Mao et al., 2017; Rainato et al., 2018), but the extrapolation of individual particle motion to total bedload transfer is subject to uncertainty. Repeated topographic surveys have also yielded information on coarse material dynamics (Lane et al., 2017; Antoniazza et al., 2019; Bakker et al., 2019; Comiti et al., 2019), but such techniques provide only coarse temporal resolution, and cannot resolve processes during transport events. Recent advances in indirect acoustic sensing have allowed substantial advances in the continuous monitoring of bedload transport in natural settings (Downing, 2010; Mizuyama et al., 2010; Rickenmann et al., 2012, 2014b; Kreisler et al., 2017; Rickenmann, 2018, 2020; Antoniazza et al., 2022). Yet, the deployment of acoustic sensors typically requires stable cross-sections (e.g. weirs) to be

mounted efficiently, which represents substantial installation costs and ecological impacts (Rickenmann, 2017), and limits the monitoring of bedload transport at multiple locations across Alpine watersheds.

Environmental seismology (Cook and Dietze, 2022) provides an alternative. Out-of-bank seismometers have been shown to record the energy emitted by bedload transport in a specific frequency band (Burtin et al., 2011; Tsai et al., 2012; Roth et al., 2016; Bakker et al., 2020). As this frequency is normally different to that associated with other fluvial processes, such as turbulence, absolute time-series of bedload transport may be inferred (Gimbert et al., 2019; Bakker et al., 2020; Lagarde et al., 2021) through the inversion of appropriate physical models (Tsai et al., 2012; Gimbert et al., 2014). Passive seismic sensors are comparatively cheap, easy to deploy in a non-invasive way and require little maintenance such that they can be distributed as networks to investigate bedload transport at multiple locations at the watershed scale (Cook et al., 2018; Coviello et al., 2019; Chmiel et al., 2022). Networks of seismic sensors have been deployed to investigate the dynamics of floods (Schmandt et al., 2017; Chmiel et al., 2022; Piantini et al., 2022), debris flows (Walter et al., 2017; Coviello et al., 2019; Chmiel et al., 2021) and glacier lake outburst floods (Cook et al., 2018; Maurer et al., 2020). To date, no study has sought to determine spatially-distributed absolute time-series of bedload transport in order to evaluate the efficiency of Alpine watersheds in conveying coarse material during a high-magnitude bedload transport event.

In this contribution, we investigate coarse material flux during a high-magnitude bedload transport event throughout an Alpine watershed. To do so, we deployed a network of 24 seismic sensors across the 13.4 km^2 Vallon de Nant watershed in the Swiss Alps, which alternates between alluvial, semi-alluvial and colluvial reaches. In a first step, we compare the absolute time-series of bedload transport obtained from a calibrated acoustic bedload monitoring device with an independent time-series of bedload transport inverted from a seismic sensor located nearby. After evaluation and confirmation of the validity, the seismic approach is used to invert time-series of bedload transport from the other 23 seismic sensors distributed across the watershed. The resulting dataset is used to investigate coarse material fluxes at the watershed scale during the studied high-magnitude bedload transport event. Combined with a morphological change analysis, we discuss the efficiency of coarse material transfers in the watershed at the scale of the studied bedload transport event, and place it into a longer time-scale perspective.

2. Material and methods

2.1 Study site

The Vallon de Nant (VdN) is a 13.4 km^2 Alpine watershed located in South-Western Switzerland (Figure 1), at ~1'200 to ~3'050 m a.s.l. Through its position at the north-western margin of the European Alps, and due to the local high relief (notably on its eastern side), it forms a natural barrier to westerly

and north-westerly air streams (Vittoz and Gmür, 2009; Lane et al., 2016). It receives a substantial amount of annual precipitation (~ 1850 mm · y^{-1}), predominantly in summer (Dutoit, 1983; Vittoz and Gmür, 2009; Lane et al., 2016; Antoniazza et al., 2022). Given its high elevation, a significant proportion (~45 % in the year 2020) of annual precipitation occurs as snowfall (Thornton et al., 2021, 2022; Antoniazza et al., 2022), and snow cover may persist until late spring-early summer in the less sun-exposed areas (e.g. valley bottom, gullies, hillslope base) of the watershed (Dutoit, 1983; Vittoz and Gmür, 2009; Lane et al., 2016; Thornton et al., 2021, 2022; Antoniazza et al., 2022). A small debris-covered glacier (Glacier des Martinets) occupies ~3% of the watershed (in 2020), supplying only negligible amounts of ice melt. Thus, the hydrological regime of the watershed is dominated by snowmelt and rainfall (Ceperley et al., 2020; Mächler et al., 2021; Michelon et al., 2021, 2022; Thornton et al., 2021, 2022; Antoniazza et al., 2022).

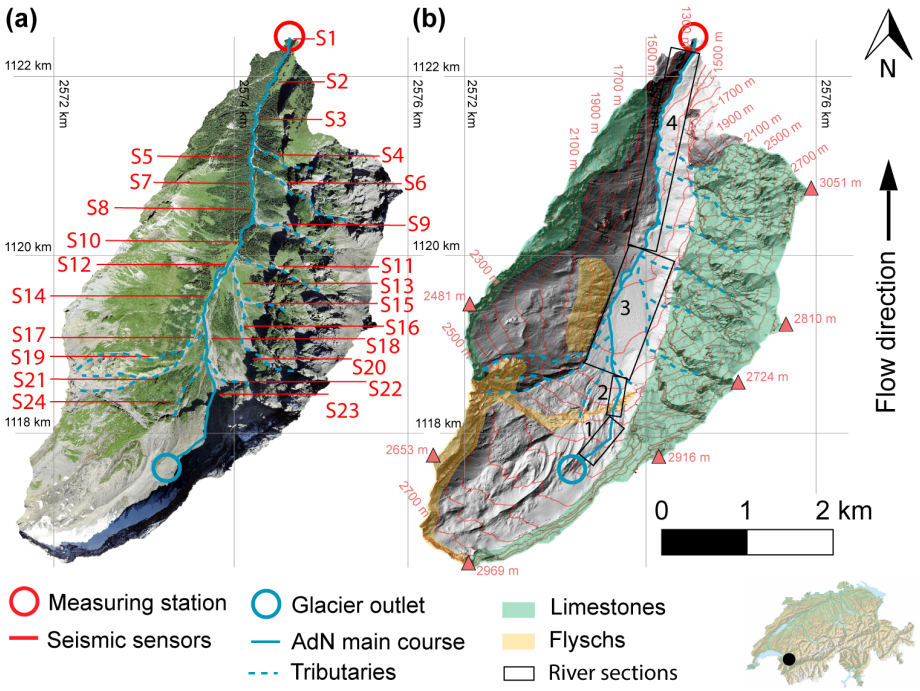

Figure 1. The Vallon de Nant Alpine watershed in (a) a 0.1-m orthophoto (2020) and in (b) a hillshade (2020) based on the the 0.5-m resolution LIDAR-based SwissAlti3d digital elevation model (Acknowledgments ©Swisstopo). Coordinates are provided in the CH1903+ Swiss system. The streamflow and SPG monitoring station at the outlet is labelled with a red circle. Seismic sensors deployed during the year 2020 are labelled S1 to S24 from downstream to upstream in (a). The Glacier des Martinets outlet and the Avançon de Nant (AdN) main course are labelled with a blue circle and blue line, respectively. The main

temporarily-flowing tributaries are labelled with a dashed blue line. In (b), the main bedrock outcrops are delineated in green (limestones of the 'Nappe de Morcles-Doldenhorn') and in yellow (flyschs of the Northern Helvetic), the rest of the surface in gray being covered by Quaternary sediment. Numbered black boxes in (b) are used to differentiate between different river sections in the text description.

Geologically, the watershed comprises rocks from the calcareous sedimentary series (limestones of Secondary age) belonging to the Helvetic domain (inverse flank of the 'Nappes de Morcles – Doldenhorn'). There are also softer North-Helvetic Tertiary flyschs outcropping locally in the southern part of the watershed (Figure 1b; Badoux, 1971; Thornton et al., 2018). Whilst limestones are subject to karstification at different rates (i.e. depending on their composition), flyschs are expected to be much less permeable, which gives the Vallon de Nant complex hydro-geological properties (Thornton et al., 2018, 2022). The geomorphology of the Vallon de Nant largely derives from its glacial legacy (Hooke, 1991; Cook and Swift, 2012; Egholm et al., 2012; Antoniazza and Lane, 2021), with a typical 'staircase' profile made of a succession of steep rockwalls and hillslopes, flatter glacier troughs, and steeper glacier riegls (Figure 1b). Bedrock only outcrops in the steeper sections (i.e. rockwalls, riegls), while the flatter sections (i.e. rockwall feet, glacier troughs) are covered by substantial depths (up to 80 m) of Quaternary till, which forms important aquifers (Thornton et al., 2022).

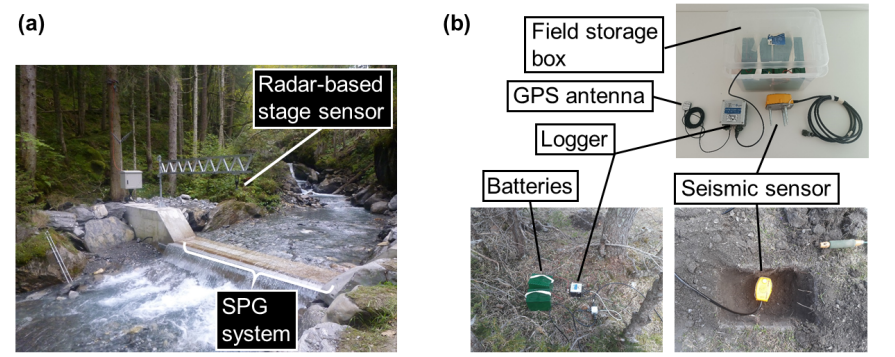

Figure 2. In (a), monitoring station at the Vallon de Nant outlet. Streamflow is continuously measured through a radar-based stage sensor, and 10 calibrated units of the SPG system provide a continuous monitoring of bedload transport. In (b), the seismic equipment (logger, sensor, GPS antenna, batteries, storage

box) used in this study, with an example of field setting.

From the glacier snout (2'313 m a.s.l.), the Avançon de Nant (AdN) flows through a glacier trough (~0.5 km, 44%; Section 1 in Figure 1b) covered by Quaternary sediment (essentially moraines with depths between 10 and 50 m; Thornton et al., 2022), then through a steeper (~0.3 km, 65%) riegl crossing a flysch outcrop (Section 2), before reaching a flatter (~1.7 km, 13%) section (Section 3) in another glacier trough, with depths of Quaternary material between 10 and 80 m (Thornton et al., 2022). Along this reach, the AdN wanders between large Quaternary coalescent alluvial fans and develops a braided morphology, as an alluvial system. At the margin of the trough, the AdN enters a more topographically-constrained section (Section 4), and alternates between semi-alluvial step-pool and alluvial wandering reaches (~ 2.9 km, 9 %). The AdN is also fed by ~10 steep (40% - 65%) tributaries (dashed blue lines in Figure 1) that are mainly active during the snowmelt season, or briefly during storm events (i.e. colluvial system), and which form large diffusive coalescent fans at the hillslope base (Lane et al., 2016; Antoniazza et al., 2022; Figure 1). They essentially feed the AdN main course in Sections 3 and 4, and alternatively cross limestone outcrops, flysch outcrops and/or Quaternary deposits (Figure 1b). Their setting may make them prone to both bedload transport events as well as debris-flow events (Rickenmann and Koschni, 2010; Lane et al., 2016).

Between 2014 and 2015, a hydrological and bedload monitoring station (Figure 2a) was built at the outlet of the watershed (1'200 m. a.s.l.; red circle in Figure 1) through a collaboration between the University of Lausanne, the Swiss Federal Institute for Forest, Snow and Landscape Research WSL, and the ETH Zürich (Physics of Environmental Systems). Since 2016, it allows for the continuous monitoring of both streamflow and bedload transport (1-min resolution), through a calibrated radar-based stage sensor, and 10 calibrated units of a Swiss Plate Geophone (SPG) system (Rickenmann et al., 2012; 2014), respectively. Antoniazza et al. (2020, 2022) and Nicollier et al. (2021a, 2022) describe the system and its calibration in detail. In this contribution, we used data from the monitoring station (i) to set the investigated bedload transport event into comparative context with other events that took place over the period 2016-2020; and (ii) as a benchmark method to evaluate the seismic inversion approach for bedload transport sensing.

2.2 Seismic inversion approach

2.2.1 Seismic monitoring

This study focuses on a high-magnitude bedload transport event that took place on August 3rd, 2020, the largest captured in the seismic time-series. In addition to the outlet SPG monitoring station, the event was simultaneously captured by a network of 24 seismic stations comprising 4.5 Hz PE6/B geophones and Cube3ext loggers (DiGOS, Germany), installed across the VdN watershed (Figure 1, Figure 2b). Sensors were installed to capture signal from the AdN main channel, and the major tributary inputs (Figure 1). Thus, the sensors covered

~9'800 m of channel length, with an average of one sensor per ~400 m of channel. One of the seismic sensors was installed next to the SPG monitoring station to be able to evaluate the performance of the seismic inversion approach in this environment. Following Bakker et al. (2020), each sensor was placed at 5-30 meters from the channel, buried at ~0.3 m underground to be isolated from surface seismic noise (e.g. rainfall, wind), oriented to the north and leveled horizontally (Figure 2b). The loggers were set to record the seismic signal with a frequency of 200 Hz, and a gain of 32. They were powered by two 9V-200Ah air alkaline batteries mounted in parallel. An internal active GPS antenna (BY-GPS-07) also recorded time continuously (Figure 2b), allowing synchronization of the measurements of the different seismic loggers, as well as data of the monitoring station (Figure 2a).

2.2.2 Seismic model application

In order to inverse bedload transport time-series from the seismic signal recorded by each sensor, a mixed turbulence (Gimbert et al., 2014) and bedload transport (Tsai et al., 2012) physical model assembled by Dietze et al. (2019) as a 'Fluvial Model Inversion' (FMI) was applied, using the R package "eseis" (v. 0.4.0) developed by Dietze (2018). The approach assumes that the seismic spectrum recorded near a river during a bedload transport event is dominated by a combination of force fluctuations in the fluid due to turbulence and coarse particles impacting the bed (Schmandt et al., 2017; Gimbert et al., 2019; Dietze et al., 2019; Bakker et al., 2020), which result in seismic power in different, yet overlapping frequency bands. The turbulence model of Gimbert et al. (2014) predicts the power spectral density (PSD) of vertical Raleigh waves induced by the flow interacting with roughness elements present along both the bed and the banks. The bedload model of Tsai et al. (2012) predicts the power spectral density (PSD) of vertical Raleigh waves generated by the impacts of saltating particles on the riverbed, assuming that the coarsest particles in transport ($> D_{90}$) are responsible for the largest seismic signal recorded (Tsai et al., 2012; Dietze et al., 2019; Gimbert et al., 2019; Bakker et al., 2020; Lagarde et al., 2021). The FMI consists in relating in a least-squared procedure the measured empirical seismic spectrum with synthetic ones produced by the paired models for random combinations of water depth h and unit bedload transport rate q_b estimated within their own plausible range, to invert the most likely values of h and q_b at each targeted time-step (Dietze et al., 2019).

Bedload transport and water depths were inverted from the paired FMI, requiring constraints on nine parameters, which can be separated into three classes following Lagarde et al. (2021); (1) the river morphology parameters, which include the channel gradient θ [radians], the channel width W [m], and the distance between the channel centerline and the seismic sensor r_0 [m]; (2) the grain-size distribution (GSD) parameters, which include the median grain-size D_{50} [m] and the standard deviation σ_g [-] of a parametric log-raised cosine function fitted to discrete measured particle classes (Tsai et al., 2012); and (3) the seismic ground properties, which are described by Green's function as (Tsai et

al., 2012; Bakker et al., 2020):

$$v_p = v_{p0}(f/f_0)^{-\xi} \text{ [1a]}$$

$$v_g = v_p/(1+\xi) \text{ [1b]}$$

$$K = K_0(f/f_0)^{\eta} \text{ [1c]}$$

where, v_p is the phase velocity of the Raleigh wave [$m \cdot s^{-1}$], v_{p0} is the phase velocity of the Raleigh wave at a frequency $f_0 = 1$ Hz, f is the frequency [Hz], ξ [-] a dimensionless exponent used to scale a frequency-dependent decay in seismic signal, v_g the wave group velocity [$m \cdot s^{-1}$], K [-] a dimensionless quality factor, K_0 [-] a dimensionless quality factor at a frequency $f_0 = 1$ Hz, and η [-] a dimensionless exponent that expresses the change in the quality factor K with frequency. To these nine site-specific parameters, two constants complete the paired FMI: the water density $\rho_w = 1000$ [$kg \cdot m^{-3}$] and the sediment density $\rho_s = 2650$ [$kg \cdot m^{-3}$].

2.2.3 Model parameterization

The river morphology parameters were derived from RTK-dGPS survey using a Trimble R10 device, combined with measurements performed on a 0.1-m orthophoto (2020) and a 0.5-m resolution Alti3d Digital Elevation Model (2020) from the aerial campaigns of the Swiss Federal Office of Topography (Swisstopo). For each of the 24 seismic stations, the position of the seismic sensor was measured to derive the sensor-to-river distance r_0; the positions of both channel edges were identified to derive the channel width W; and the average channel gradient θ was computed over a reach of ~100 m encompassing the seismic sensor location. The coordinates of the 24 seismic sensor locations, together with the river morphology parameters measured at each site, are available in Supporting information S1 (Table S1).

The grain-size distribution parameters were derived from a line-by-number count (Wolman, 1954; n = 100) of mobile particles on the riverbed (Bakker et al., 2020; Lagarde et al., 2021) performed at each of the 24 seismic sensor locations. The particles were then separated into 10 size classes (Bakker et al., 2020; Supporting Information S2), and the parameters D_{50} and σ_g were derived following Tsai et al (2012) from a best-fit log-raised cosine function out of $n = 10^4$ runs. The grain-size distribution parameters measured at each of the 24 seismic sensor locations are available in Supporting Information S2 (Table S2; Figure S2).

The seismic ground property parameters were derived from an active seismic survey undertaken individually for each seismometer following Bakker et al. (2020). First, a second seismic sensor was installed on the opposite bank from a given seismic station targeted for the ground seismic parameterization. Both loggers were set to record at 800 Hz in order to capture the active seismic signal at the highest possible rate. A metallic plate with dimensions 0.3 m x 0.3 m x 0.01 m (thickness) and a mass of ~15 kg was set in line with the two seismic stations, and its position was recorded using a RTK-dGPS Trimble R10 device. The line

made by the two seismic stations and the impact plate was orthogonal to the streamflow, and the impact plate was set at one end of the line. During periods of low streamflow to minimize signal contamination by turbulence, the plate was repeatedly struck 20 times using a sledgehammer, in order to derive for each impact the decay in surface wave velocity v_g with frequency, according to the arrival time of the active seismic signal at the two sensors. To do so, we first deconvolved the raw seismic signal according to the sensor characteristics. We also removed the mean and the seismic signal was detrended to avoid artifacts in the calculation of the power spectral density function (Lagarde et al., 2021). Following Bakker et al. (2020), the seismic signal was band-pass filtered for 50% overlapping intervals of 6 Hz, and a Hilbert envelope was calculated to identify the signal peak amplitude of each hammer blow. Knowing both distance and arrival time delay (i.e. in peak amplitude) between the active seismic source and the sensors, the surface wave velocity v_g was derived, and its decay with frequency allowed to constrain parameters v_{p0} and ξ in equations [1a] and [1b].

Second, the position of the impact plate was changed multiple times (~4-10) to vary the distance (~5-100 m) between the seismic sensor and the active seismic source. At each impact location, the position of the plate was measured using an RTK-dGPS Trimble R10, and 20 consecutive impacts were performed using a sledgehammer. This experiment was used to quantify the attenuation in seismic power with distance to the seismic source K (or quality factor, equation [1c]), and assess its frequency dependency (η in equation [1c]). To do so, signal spectrograms were computed from the detrended seismic signal using the Welch's method (Welch, 1967), averaging seismic power at 1 s intervals using 80% overlapping sub-windows of 0.5 s.

The active seismic experiments were repeated at each seismic sensor location to derive site-specific ground seismic properties, with the exceptions of sensor groups S10-S12, S16-S20 and S22-S23-S24, where a single active seismic experiment encompassing each group of sensors was performed, thanks to their geographical proximity. Parameters v_{p0} and ξ from equations [1a] and [1b], and parameters K_0 and η from equation [1c], estimated at each of the 24 seismic sensor locations based on active seismic experiments, are reported in Supporting Information S3 (Table S3, Figure S3a and S3b).

2.2.4 Model application

Using the parameters determined in 2.2.3, combined with range of plausible water level h (0.1 to 1 m) and unit bedload transport rates q_b (10^1 to 10^5 $kg \cdot min^{-1}$) estimated from the monitoring station data, $2 \cdot 10^4$ synthetic spectra are produced in the FMI, and compared to the empirical spectrum in a least-squared procedure (Dietze, 2018; Dietze et al., 2019). Doing so, the values of h and q_b minimizing the error between the synthetic and the empirical spectra are determined at 1-min resolution. Since we are interested in bedload transport, the inversion is performed focusing on a range of frequencies (25-60 Hz) in which bedload noise is normally found (Tsai et al., 2012; Schmandt et al., 2017; Bakker et al., 2020), optimizing the inversion of q_b at the expense of h. We

do not further consider the inversions of h in the frame of this study. This procedure is applied to every sensor, providing with 24 absolute time-series of bedload transport, at 1-min resolution, over the duration of the 3rd of August 2020 event and distributed across the Vallon de Nant watershed.

2.3 Data analysis

2.3.1 Evaluation of the seismic inversion approach

The seismic inversion approach was first applied to the data recorded by the seismic sensor that was located near to the SPG monitoring station (~20 m). Doing so, the seismically-inverted flux could be compared to a second and independent measurement of bedload transport over the event of interest, allowing assessment of the performance of the inversion approach. After evaluation, the same seismic inversion approach was then applied to the other 23 sensors distributed in the VdN watershed but using the site-specific parameters following the procedure described in 2.3.3 and 2.3.4. The site-specific parameters are reported in Supporting Information S1, S2 and S3.

2.3.2 Spatially-distributed seismic monitoring of bedload transport

Once the inversion procedure was applied to the 24 seismic sensors, spatially-distributed time-series of bedload transport for the event of interest were obtained. Three statistics were used to characterize the bedload transport event measured at each sensor location: (1) the mass of bedload transported over the event duration; (2) the timing of the start and end of the bedload transport event, and the timing of the major (multiple hours in duration) bedload transport waves; and (3) the lag and propagation velocity between spatially-consecutive bedload transport time-series.

Objective criteria applicable to every time-series were used to automatically determine these statistics. An example of how this was done is provided in Figure 3 for sensor S1 located near to the monitoring station and where two major bedload transport waves were identified. Note that two major bedload waves were identified on the majority of the seismic sensors (20 out of 24), one sensor (S19) recorded only one major bedload transport wave and one sensor (S6) recorded three of them. The remaining two sensors (S9 and S15) recorded no bedload transport.

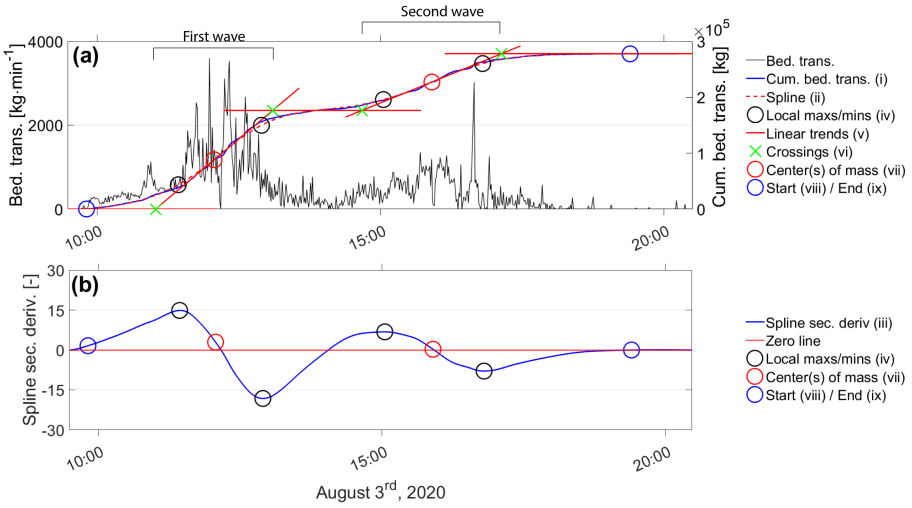

Figure 3. Example of the procedure applied to each of the 24 seismic-inverted bedload transport time-series to determine: (1) the mass of bedload transported over the event duration; (2) the timing of the bedload transport event starting and ending points, and the timing of the major (multiple hours in duration) bedload transport waves; and (3) the lag and propagation velocity between spatially-consecutive bedload transport time-series. The example is provided for seismic sensor S1 located near to the monitoring station.

At step (i), we calculated a cumulative sum of bedload transport rates over the duration of the bedload transport event for each sensor (blue line in Figure 3a). At step (ii), we fitted a smoothing spline to each cumulative distribution (dashed red line in Figure 3a). At step (iii), we calculated the second derivative of the spline (blue line in Figure 3b) to obtain (iv) inflexion points (i.e. local maxima and minima in the second derivative; black circles in Figure 3a and 3b). At step (v), we calculated the equation of the lines meeting each pair of consecutive inflexion points (red lines in Figure 3a). The slope coefficient of the lines before, in-between and after any bedload wave was set to zero, and the crossing points between trend lines (green crosses in Figure 3a) was retained as the start and end points of each major bedload wave (vi). At step (vii), we computed the center of mass of each major bedload wave (red circles in Figures 3a and 3b), by taking the mid-point between trend line crossings marking a linear increase in the spline fit. At step (viii), the starting point of the bedload transport event was set at the crossing between the spline fit and bedload transport rate zero line. At step (ix), the end of the bedload transport event was determined as the point from which the spline fit reaches an upper plateau (i.e. a second derivative greater than -0.01; blue circles in Figures 3a and 3b).

Integration of the bedload transported mass between the start (vii) and end points (viii) gave us (1) the bedload mass transported over the duration of the event at each seismic sensor location. It allows quantification of the change

in the transported bedload mass across the watershed during the studied bedload transport event, and the relationship between the transported mass and contributing area (measured on a 0.5-m digital elevation model of 2020). The timing of the bedload transport start (vii) and end (viii) points, as well as the timing of the major bedload transport waves (vi), allowed us to calculate (2) to compare the timing of the bedload transport event at the different seismic sensor locations. To characterize the temporal lag between time-series of bedload transport measured at two spatially consecutive seismic sensors, and the associated propagation velocity, a cross-correlation analysis was performed. Using the distance between two spatially consecutive sensors measured on a 0.1-m orthophoto of 2020, propagation velocities between pairs of spatially-consecutive sensors were computed to obtain (3).

2.3.3. Morphological change analysis

In order to place the 3rd of August 2020 bedload transport event into a longer-term perspective of sediment fluxes throughout Alpine watersheds, we perform a morphological change analysis. It is derived from two 0.5-m resolution LIDAR-based (Swisstopo aerial campaigns) SwissAlti3d digital elevation models (DEM) of 2016 (August 25th) and 2020 (August 6th). By subtracting their altitude cell-by-cell, erosion and deposition depths across the watershed area are obtained over the survey interval, and volumetric changes can be obtained by multiplying cumulated vertical changes ($>$ 0.1 m and $<$ -0.1 m) by the DEM cell resolution (0.5 x 0.5 m). Patterns of erosion and deposition encompass the effects of the 3rd of August 2020 bedload transport event, but also multiple other bedload transporting events that have taken place in this time interval (Antoniazza et al., 2022). Note that while seismic sensing measures bedload transport only, morphological change analysis may also include finer material transported in suspension.

3. Results

3.1 The August 3rd 2020 bedload transport event

The August 3rd 2020 bedload transport event was the largest one recorded during the year 2020 at the outlet monitoring station, with a peak water depth of 0.39 m (4.3 $m^3 \cdot s^{-1}$), and a peak of bedload transport of 1240 $kg \cdot min^{-1}$ measured simultaneously (~12:15). Over its duration (Figure 4), ~73'700 kg of bedload were exported at the outlet according to the SPG recording, which represents 11% of the bedload that was transported over the year 2020 (Antoniazza et al., 2022). In comparison to the period 2016-2020 analyzed by Antoniazza et al. (2022), the 3rd of August 2020 flood is the 5th largest in terms of bedload transport rate peak, the largest being monitored on August 6th 2018, with a bedload transport rate peak measured at 3540 $kg \cdot min^{-1}$. Meteoswiss datasets RhiresD and TabsD (MeteoSwiss, 2017, 2019) of daily precipitation and daily mean temperature show that 57.4 mm of precipitation (with a mean daily temperature of 5.75°C) fell over the Vallon de Nant on August 3rd 2020, likely as rainfall given the $>$ 1°C daily mean temperature. The hydrological analysis

performed by Antoniazza et al. (2022) further indicates that daily melt cycles on August 3rd, 2020 (outside of rainfall events) were visible in the flow hydrograph, meaning that a signal related to snowmelt was present in the watershed, and that baseflow was still relatively high (~0.5 $m^3 \cdot s^{-1}$). Heavy rainfall and high baseflow thus combined to produce a rapid increase in streamflow (Figure 4), with two successive waves between 11:00 and 13:00, and between 15:00 and 18:00 on August 3rd. Generally, bedload transport followed the same trend as streamflow, with two larger waves taking place with a comparable timing to streamflow peaks on August 3rd.

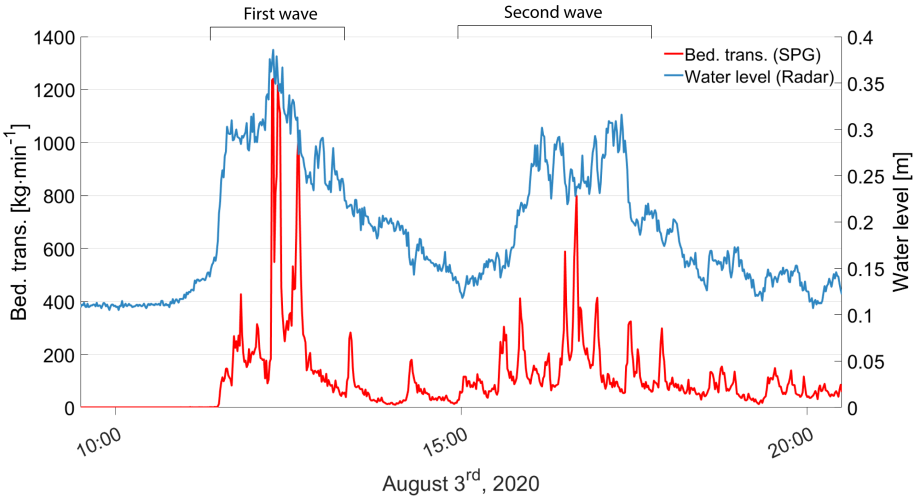

Figure 4. The 3rd of August 2020 bedload transport event measured at the Vallon de Nant outlet monitoring station. Bedload transport time-series measured with the 10 calibrated SPG units is plotted (in red) together with the radar-based water level time-series (in blue).

3.2 Evaluation of the seismic inversion approach

At the seismic sensor located close to the SPG monitoring station, the dGPS-RTK survey combined with GIS measurements gave a channel width of W = 6 m, a channel gradient θ = 0.06 radians, and a distance between the seismic sensor and the river centerline r_0 = 5 m. The application of a best-fit log-raised cosine function to a line-by-number count of riverbed mobile material gave D_{50} = 0.06 m, and σ_g = 0.9 (Figure 5a).

Data from the active experiment were then used to derive the seismic ground property parameters v_{p0}, ξ, K and η in equations [1a], [1b] and [1c]. The decay in wave group velocity with frequency between the two seismic loggers spaced 12 m away on opposite banks was found to be best expressed with v_{p0} = 482 $m \cdot s^{-1}$ and ξ = 0.25 (Figure 5b), by combining equations [1b] and [1c]. These values are close to, though a bit lower, than the ones found by Bakker et al. (2020) for a similar active seismic experiment conducted in an alluvial channel; but

substantially lower than the ones proposed by Tsai et al. (2012) for a generic bedrock site (Figure 5b). Seismic power rapidly decreased with distance at the different frequencies towards background signal level (Figure 5c). Change in the quality factor K with frequency was estimated using equation [1c], and gave K_0 = 17.3 and $\eta = 0.14$ (Figure 5d). The frequency dependency of K is not very strong, which is consistent with the constant value of $K = 20$ proposed by Tsai et al. (2012). The value of the exponent $\eta = 0.14$ is also close to the one found in Bakker et al. (2020) for an alluvial channel ($\eta = 0.15$; Figure 5d).

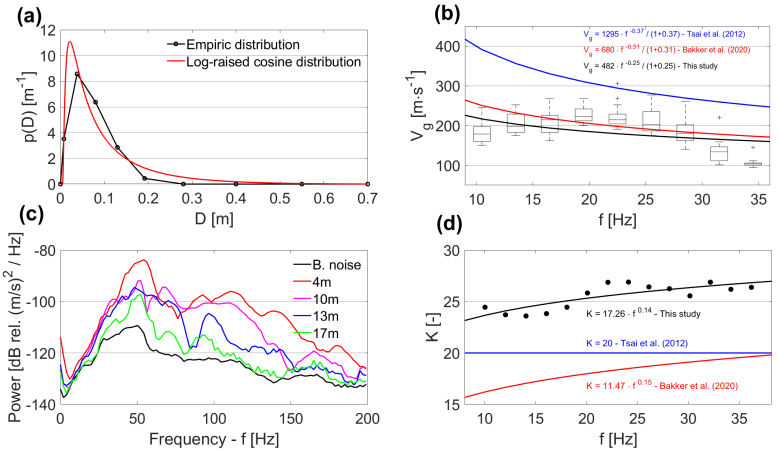

Figure 5. Parameter estimate for the seismic sensor S1 located close to the SPG monitoring station (see also Figure 1). In (a), best-fit log-raised cosine function applied to a line-by-number count of mobile bed material (n = 100), to derive parameters D_{50} and σ_g. In (b), decay in wave group velocity with frequency between two seismic sensors located on opposite banks. The boxplots show the variability for 20 repeated impacts with a sledgehammer. The regression curve (black) describes the wave group velocity decay with frequency, based on equations [1a] and [1b], and the parameters found by Bakker et al. (2020) for an alluvial channel (in red), and proposed by Tsai et al. (2012) for a generic bedrock site (in blue), are presented for comparative purpose. In (c), attenuation of seismic power with distance. Lines represent the average of 20 repeated impacts using a sledgehammer (i.e. without including pauses between sledgehammer blows), and the line in black shows the background noise of periods without active seismic experiment. In (d), change in the quality factor K with frequency according to equation [1c]. The parameters found by Bakker et al. (2020) for an alluvial channel (in red), and proposed by Tsai et al. (2012) for a generic bedrock site (in blue) are presented for comparative purpose.

Following the field-based estimation of the nine parameters in the FMI, the time-series of bedload transport were inverted (Figure 6). The August 3rd 2020 bedload transport event is well visible on the seismic power spectrogram (Figure 6a), with two consecutive periods (11:00-13:00 and 15:00-18:00) recording

substantially more seismic energy (i.e. > -110 dB) than the preceding (09:30-11:00), interceding (13:00-15:00) or following (18:00-20:30) ones. In Figure 6b, the results of the bedload transport seismic inversion are presented (in black), together with the time-series of bedload transport (SPG measurement, in red) and of water depth (radar measurement, in blue). Results of the inversion show that the seismic-based time-series of bedload transport varies together with changes in the seismic power, with bedload transport rate being low during periods of weak seismic energy and peaking up to 2740 kg $\cdot$ min^{-1} at its maximum (12:18).

The general trend of the bedload transport event sensed with the SPG monitoring system is identified by the bedload seismic inversion (Figure 6b). On August 3rd 2020 both monitoring systems recorded a first wave with greater peak at 11:00 – 13:00, and a second with smaller peak at 15:00 – 18:00. Outside of these periods of high bedload activity, both monitoring systems measured no or little bedload transport (e.g. 18:00-20:30). The timing of the greater bedload transport peaks (seismic-inverted bedload transport > 1000 kg $\cdot$ min^{-1}) is relatively synchronous for both monitoring systems: there are 3 minutes of lag in the peak of the first major bedload transport wave (~ 12:15), and 1 minute of lag in the peak of the second major bedload transport wave (~ 16:40), while both waves last multiple hours. For the second major bedload wave (16:00 – 18:00), the radar-based water level sensor measures multiple high peaks in streamflow, while both bedload transport monitoring systems recorded a higher transport peak occurring in-between in a period of relatively lower streamflow (at ~ 16:40). This confirms in this instance that the FMI is indeed able, based on different frequency bands, to differentiate between seismic sources related to either water or bedload transport, and that inverted bedload transport is not only a function of increasing water depth and increasing turbulence rate.

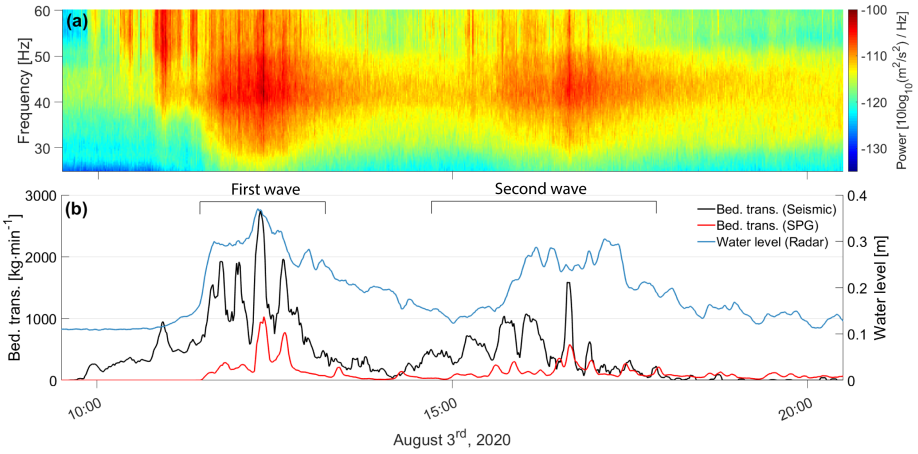

Figure 6. In (a), seismic power spectrogram of the 3rd August 2020 bedload transport event for the seismic sensor S1 located close (~20 m) to the SPG monitoring station. In (b), bedload transport time-series (in black) inverted

using the FMI constrained with the nine field-based parameter estimates. The bedload transport time-series measured at the SPG monitoring station is also provided (in red) for evaluation purposes, as well as the water level time-series measured with the radar-based stage sensor (in blue). Note that a 5-min moving average has been applied to all three time-series.

The seismic inversion of bedload transport generally tends to overestimate the SPG-derived bedload fluxes, to a factor of 4 on average for bedload transport rates greater than 60 $kg \cdot min^{-1}$ (1 $kg \cdot s^{-1}$). Over the duration of the bedload transport event, ~50 % of the 1-minute data points are below a factor 3 of difference, and the two previously identified bedload peaks (~12:15 and ~16:40) both present a factor 2.7 of difference. The measurement of bedload is expected to become more uncertain towards low transport rates, especially around the threshold of motion, for both measuring systems. This is notably visible at the beginning of the flood (10:00-11:00), where the seismic-inverted bedload flux rises substantially, while the SPG monitoring measures no bedload transport. Over the duration of the bedload transport event (Figure 6), the seismic inversion of bedload transport gives a total transported mass of 2.8 $\times 10^5$ kg, which represents in average a factor 3.8 of difference (74 % greater) compared to the 0.74 $\times 10^5$ kg measured by the SPG system.

3.3 Spatially-distributed bedload transported mass

The seismic power spectrograms of every sensor (columns 1 and 3 in Figure 7) show more seismic energy recorded on August 3rd between 11:00 and 18:00, as compared to preceding and following periods. In most instances, two distinct periods of higher seismic energy (11:00 – 13:00 and 15:00 – 18:00) corresponding to the two bedload waves identified in Figure 6, are observable (e.g. S1, S3, S5, S6, S7, S8, etc.). Sensors close to the continuously flowing main channel (e.g. S1, S2, S3, S5, S7, S8, S10) tend to record more seismic energy throughout the period due to permanent turbulence, as compared to temporally-flowing tributaries (e.g. S4, S6, S9, S15, S19), which only show higher seismic energy during discrete hydrological events. Seismic power spectrograms may not be directly comparable to each other due to site-specific differences (e.g. ground seismic properties, distance to seismic source), which are not yet taken into account at this stage of the processing. For instance, sensor S12 – located along the main channel – seems to record relatively little seismic energy, but this is likely because it was positioned relatively far (~30 m) from the flow.

Figure 7 (columns 2 and 4) shows the results of seismic inversion. The two bedload waves identified in Figure 6 at sensor S1 are visible – with differences in timing and magnitude at S2, S3, S7, S8 and S10 (upper limit of the semi-alluvial Section 4 in Figure 1). From S10 on, it becomes harder to track the bedload waves since the main channel is now fed by multiple tributaries draining relatively large sub-catchments (Figure 1). The two waves are nevertheless visible at S12, S13, S14, S16, S17, S21 and S22. While large bedload waves were sensed in some tributaries (e.g. S4, S6, S11, S16, S17), no or little bedload transport was measured within others (e.g. S9, S15, S19). Although no bedload

transport was inverted for S9 and S15, higher seismic energy is visible at the timing of the bedload transport event. As its frequency was outside of the bedload-specific bands, this is likely related to passage of a bedload-free water wave.

The time-series of bedload transport are combined into sub-catchment groups (a-f) in Figure 8, to visualize bedload transport patterns throughout the watershed, and the mass of bedload transported over the duration of the event is presented in the associated Figure 9. Starting from upstream, two sub-catchments (d, f) recorded large amounts of bedload ($> 10^6$ kg), in particular measured at sensors S16, S17 and S21. In contrast, substantially less bedload (10^5 – 5×10^5 kg) was transported through sub-catchment (e), which drains the upper watershed area (i.e. where the glacier lies; Section 1 in Figure 1). In sub-catchment (d), the large amount of bedload ($> 10^6$ kg) measured at S21 and S17 seem to be already substantially attenuated at S14 (10^5 – 5×10^5 kg). In sub-catchment (e), bedload is supplied from three different tributaries, and less bedload is transported downstream of their confluence at S18. In sub-catchment (f), bedload transport increases from S20 (5×10^5 – 10^6 kg) to S17 ($> 10^6$ kg), before decreasing at S13 (5×10^5 – 10^6 kg), with no tributary input from S15. In sub-catchment (c), larger amounts of bedload are transported at S13 (5×10^5 – 10^6 kg) supplied from sub-catchment (f), than there are at S14 (10^5 – 5×10^5 kg) supplied from sub-catchments (d) and (e) combined. There is still a substantial amount of bedload transported at S12 (5×10^5 – 10^6 kg), which drains all sub-catchments (d), (e) and (f). Although bedload transport at S12 combines with a significant tributary input coming from S11 ($> 10^6$ kg), substantially less bedload is transported at S10 (10^5 – 5×10^5 kg) at the downstream end of sub-catchment (c), which also corresponds to the end of the braided river reach (Section 3 in Figure 1).

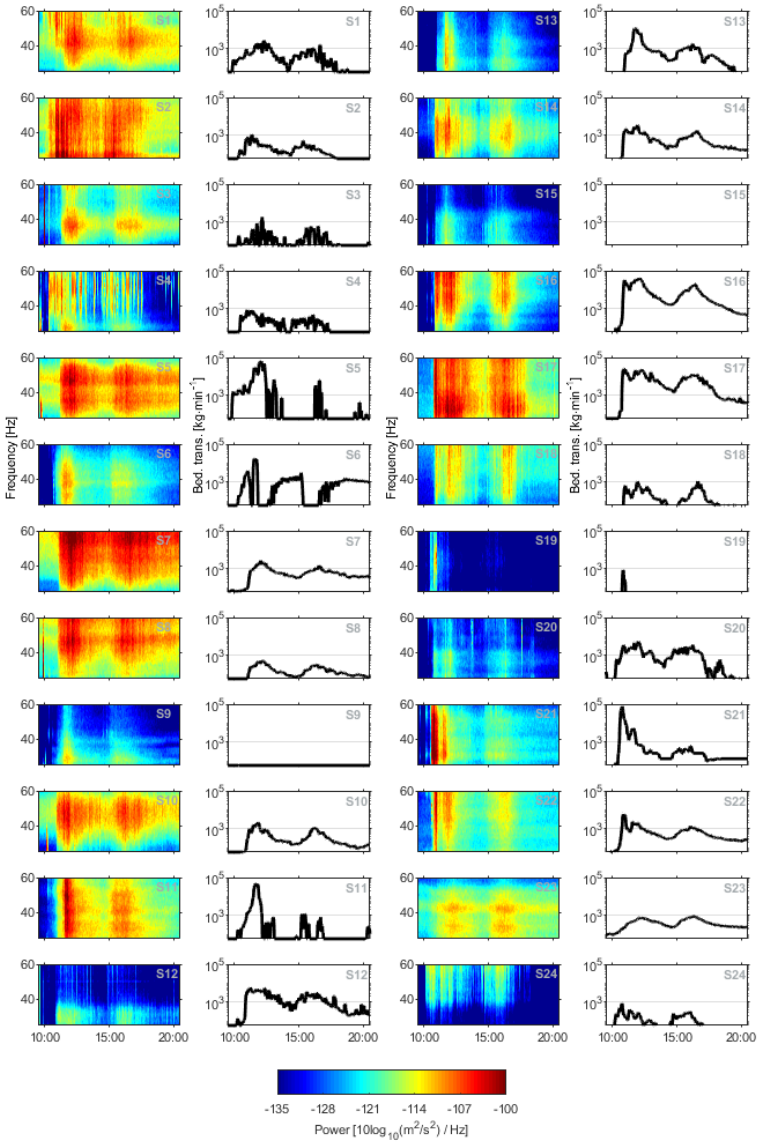

Figure 7 (above). Seismic power spectrograms and seismic-inverted bedload transport time-series for the 24 seismic sensors distributed in the Vallon de Nant Alpine watershed. The inversion focuses on the bedload transport event that took place on August 3rd 2020.The seismic sensors are labelled S1 to S24 from downstream (the SPG monitoring station) to upstream (Figure 1). Note the y-axis log-scale in the seismic-inverted bedload transport time-series, and that

a 5-min moving average has been applied to time-series of bedload transport.

There is comparatively less bedload transported throughout sub-catchment (b), where different sensors (S10, S8, S7) measured between 10^4 and 5 $\times 10^5$ kg of material. Heading downstream over consecutive sensors, there is more bedload material measured at S10, less at S8 and more again at S7, with no tributary input from S9, which confirms that erosion also takes place. There is another substantial tributary input from S6 (5 $\times 10^5$ - 10^6 kg), which combines with supply from S7 in the main channel (10^5 – 5 $\times 10^5$ kg) to produce an important bedload flux at S5 in the main channel ($> 10^6$ kg). This large sediment flux rapidly attenuates throughout sub-catchment (a), where 10^4 – 5 $\times 10^5$ kg of material are measured over the different sensors (S1, S2, S3). Again, a greater mass of bedload transport is measured at S1 and S2 as compared to S3 located upstream, which emphasizes the occurrence of erosion.

If we take within each headwater tributary the sensor that has recorded the greatest mass of material over the duration of the event (i.e. sensors S4, S6, S11, S16, S17, S22, S23 and S24), and sum their respective mass, we can state that a minimum of 1.1 $\times 10^7$ kg of bedload material was mobilized in the headwater channels during the 3rd of August 2020 bedload transport event. In comparison, only 2.8 $\times 10^5$ kg is exported at the outlet (sensor S1), which represents 2.5 % of what has been mobilized. This is a minimal estimate, since it assumes that only deposition took place downstream of the headwater sensors, while evidence of erosion (greater bedload mass at downstream sensors compared to upstream ones) has also been observed (e.g. between S8 and S7, between S3 and S2). In addition, we do not know if the bedload material measured at two consecutive sensors is the same, and in what proportion, or whether deposition and erosion also occurs in-between sensors. Thus, it is likely that an even lower proportion of the total amount of bedload mobilized through the watershed is actually exported at the outlet. Note that we do not find any obvious difference in the mobilized amount of material between the tributaries draining the flysch outcrops (e.g. S19, S21, S23 and S24), or the ones draining limestone outcrops (e.g. S20, S11, S6), suggesting the likely prominent importance of local material availability, either from bedrock weathering or Quaternary-deposited stocks.

Channel gradient, contributing area, the bedload mass transported over the duration of the event and the transported bedload mass per unit area at each of the 24 seismic sensor locations are presented in Figure 10, along with the relationships between contributing area and the transported bedload mass. The data presented in Figure 10 are available in Supporting Information S4. Channel gradient is lower within the main channel (e.g. S1, S3, S5, S7, S10), and greater in the tributaries feeding it (e.g. S4, S6, S9, S11). Gradient also tends to increase towards the watershed head, where multiple steeper tributaries combine to form the AdN main channel (Figure 1; Figure 10a). Contrastingly, contributing area decreases upstream (Figure 10b), and seismic sensors located within the AdN main channel drain a much larger area than the tributaries feeding them. There is a negative power law relationship between gradient (G) and contributing area

(CA), such as $G = 23 * \mathrm{CA}^{-0.33}$ ($\mathrm{R}^2 = 0.71$).

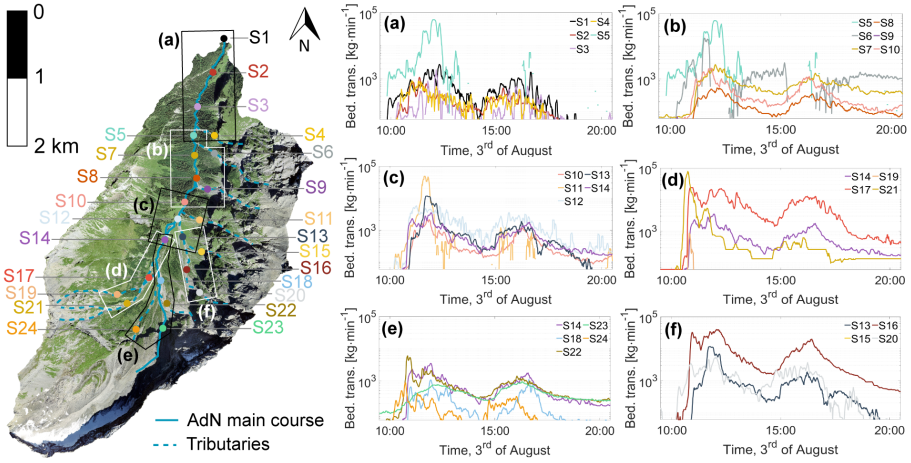

Figure 8. Time-series of bedload transport on August 3rd 2020 (09:30 – 20:30) for the 24 seismic sensors deployed in the Vallon de Nant Alpine watershed. The dots represent the location of the seismic sensors and their color corresponds to the color of the time-series of bedload transport in the graphs to the right. Time-series of bedload transport are combined into sub-catchment groups (a-f) to better visualize how bedload moves through the watershed. Note that a 5-minutes moving average has been applied to time-series of bedload transport. Acknowledgments ©Swisstopo.

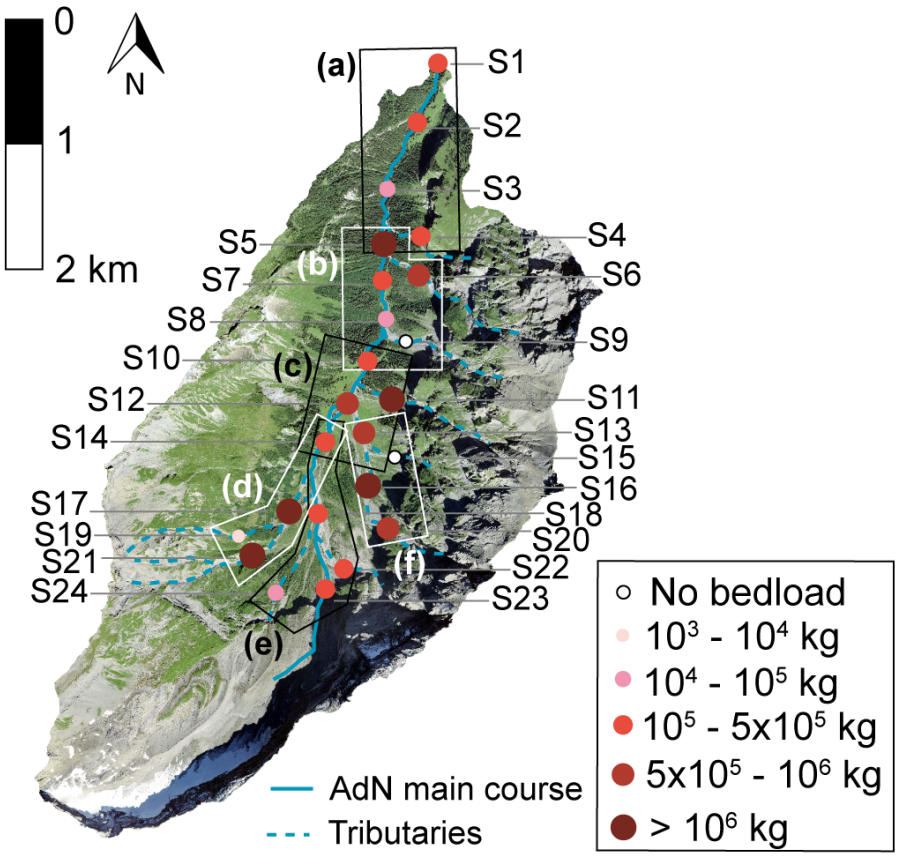

Figure 9. Mass of bedload transported over the duration of the 3rd of August 2020 bedload transport event in the Vallon de Nant Alpine watershed, at the 24 locations where a seismic sensor was deployed. Time-series of bedload transport are combined into sub-catchment groups (a-f) to better visualize how bedload moves through the watershed. Acknowledgments ©Swisstopo.

As observed in Figure 8 and 9, both the transported bedload mass (Figure 10c) and the transported bedload mass per unit area (Figure 10d) tends to be greater in the steep tributaries (e.g. S4, S6, S11, S16, S17) as compared to the AdN main channel (e.g. S1, S2, S3, S7, S8, S10), which suggests a strong filtering of the bedload signal between the headwater tributaries and the watershed outlet. This observation is confirmed by a negative power law relationship ($R^2 = 0.13$) between contributing area and the bedload mass transported over the duration of the event (Figure 10e). The relationship is nevertheless made more complex by high rates of material supply from tributaries into the main channel (e.g. S6 S5), and by varying mass of material transported throughout different portions of the watershed, also reflecting differences in local sediment availability.

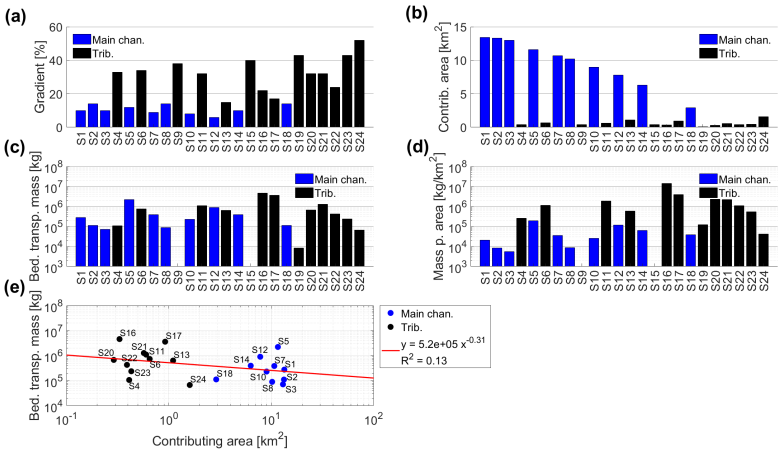

Figure 10. Gradient (a), contributing area (b), bedload transported mass over the duration of the event (c), and transported bedload mass per unit area (d) at each of the 24 seismic sensor locations. In (e), relationship between contributing area and the bedload mass transported over the duration of the event.

3.4 Spatially-distributed bedload transport timing

The start and end of bedload transport (blue circles) and the timing of the major bedload transport waves (red circles) at each seismic sensor location are presented in Figure 11a. Starting from upstream, the bedload transport event begins relatively synchronously on the headwater tributaries (S19 to S24), at ~10:00 on August 3rd. The timing of the bedload waves indicates an earlier activity in sub-catchment (d) at S19 (i.e. one wave at 10:54) and S21 (i.e. two waves at 10:49 and 14:55), as compared to sub-catchment (f) (i.e. two waves at 11:44 and 15:44). The different headwater tributaries in sub-catchment (e) show a substantial variability in the timing of the bedload transporting event, with the two waves occurring earlier at S24 (i.e. 11:15 and 15:34), then at S22 (i.e. 11:32, 16:21), and finally at S23 (i.e. 12:24 and 16:39). The tracking of the bedload transport event downstream from headwater tributaries is made more complex by the multiple tributaries transporting different amounts of sediment at different times, over river reaches of different lengths and with different transport efficiency. A general lag in downstream direction (decreasing from S24) in the timing of the bedload starting point, and in the timing of the two major bedload waves, is observable in Figure 11a, notably in the upper part of the watershed (sensors S24 to S7).

Figure 11b presents the inter-sensor distance [m] (up left), the lag between two consecutive bedload transport time-series [min] (up right), the maximum r-values [-] corresponding to that lag (bottom left), and the associated propagation velocity [m · min^{-1}] (bottom right). The data in Figure 11b are available in Supporting Information S5. Cross-correlation analysis shows a rapid propagation of the bedload transport event through sub-catchment (d), with velocities of 97

$m \cdot min^{-1}$ between S19 and S17 (r = 0.35) and of 28 $m \cdot min^{-1}$ between S21 and S17 (r = 0.48). The bedload transporting event also propagates rapidly through sub-catchment (f), with a velocity of 57 $m \cdot min^{-1}$ between S20 and S16 (r = 0.89). In sub-catchment (e), smaller propagation velocities (10 $m \cdot min^{-1}$) were estimated from S24 to S18 (r = 0.78), and higher ones (41 $m \cdot min^{-1}$) between S22 to S18 (r = 0.72). The bedload transport event occurs almost synchronously at S18 (two waves at 12:07 and 16:39) and at S23 (i.e. two waves at 12:24 and 16:39; Figure 11a), whilst they are located 651 m away. Either S18 is first supplied by S24 and S22 which showed an earlier activity, or local hydrological and sediment availability conditions generate a mobilization that may be, at least partly, independent from the upstream event propagation.

(a)

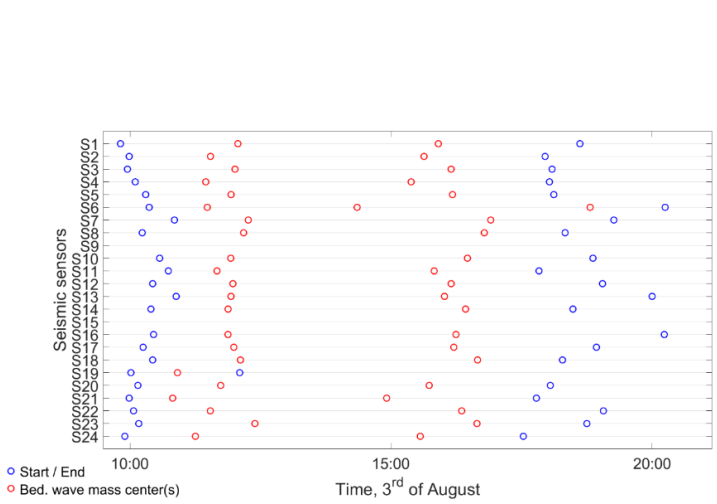

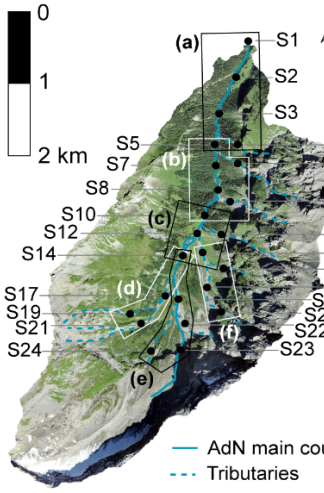

(b)

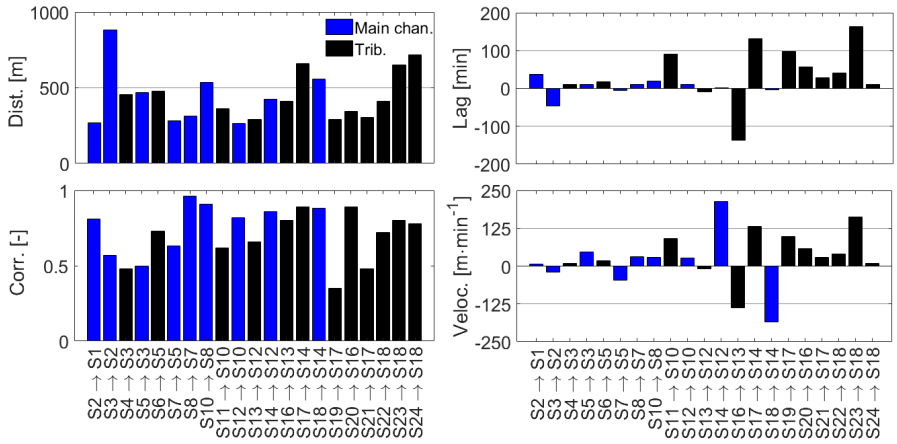

Figure 11. In (a), start and end of the bedload transporting event (blue circles) and timing the major bedload transport waves (red circles) measured at the 24 seismic sensor locations, from upstream (S24) to downstream (S1). In (b), inter-sensor distance [m] (top left), estimated lag [min] between time-series of bedload transport measured at two spatially-consecutive seismic sensors (top right), and associated correlation r-values [r] (bottom left), as well as estimated bedload transport velocity [$m \cdot min^{-1}$] between sensor pairs (bottom right). Acknowledgments ©Swisstopo.

The bedload transporting event propagates very rapidly between S17 and S14 (132 $m \cdot min^{-1}$, r = 0.89), which also raises the question whether a spatially-continuous propagation of the event from upstream is reasonable. A later activity at S18 as compared to S17 and S14 (i.e. two waves at 11:43 and 16:26) suggests that S14 at the downstream end of sub-catchment (d) is first supplied by S17, and later by S18, which explains the negative velocity measured between S14 and S18. In the downstream part of sub-catchment (e), the bedload transport event occurs almost simultaneously at both S16 and S13, while they are located 411 m away. The same observation is to be made for sensor pairs S12 and S14, where a short 2-min lag has been measured between sensors spaced 426 meters away, which may also explain the negative velocity measured between S12 and S13. A 10-minute lag is measured between S10 and S12 spaced 263 m away, which gives a velocity of 26 $m \cdot min^{-1}$ (r = 0.82). S10 is also fed by a tributary input from S11, which shows a high velocity 91 $m \cdot min^{-1}$ (r = 0.62). Earlier activity at S11 suggests that S10 may be first supplied by the tributary, and shortly after by S12 in the main channel (Figure 11a).

The propagation of the bedload transport event downstream from S10, to S8 and S7, shows a clear consistency, with velocities of 28 $m \cdot min^{-1}$ (r = 0.91) and 31 $m \cdot min^{-1}$ (r = 0.96), respectively. A negative velocity is then measured between S5 and S7, and is likely related to an earlier activity in tributary S6 (i.e. waves at 11:29 and 14:21), which supplies material to S5 (18 $m \cdot min^{-1}$, r = 0.73) before the bedload transport from the main channel at S7 (i.e. waves at 12:16 and 16:54) makes it to S5 (i.e. waves at 11:56 and 16:11). A similar early supply from tributary S4 (i.e. waves 11:27 and 15:23) to S3 (10 $m \cdot min^{-1}$, r = 0.5) in the main channel (i.e. waves at 12:01 and 16:09) suggests that S3 is first supplied by the tributary input from S4, and later on by material from the main channel at S5. Sensor S2 shows an earlier activity (i.e. waves at 11:32 and 15:38) than sensors located upstream from it, which result in a negative propagation velocity, and also questions the likelihood of a spatially-continuous downstream propagation. Downstream propagation from S2 to S1 (i.e. waves 12:04 and 15:54) results in a velocity of 7 $m \cdot min^{-1}$ (r = 0.81).

3.5 Longer-term morphological change analysis

Morphological change during the period 2016-2020 (Figure 12) shows a clear melt and subsidence of the glacier area in the upper watershed (i.e. not accounted in volume change estimates to only focus on sediment erosion and deposition). Substantial erosion is visible in a number of steep gullies feeding the

tributaries, notably upstream of S4, S6, S9, S11, S15, S21 and S22. Patches of erosion with substantial depths (i.e. meters) are visible high up in the rock-walls, notably on the eastern face of the Vallon de Nant Alpine watershed. In this tributary-dominated area (zone 'i' in Figure 12 and Table 1), 4.978×10^5 [m^3] of material were eroded during the period 2016-2020, which represents 98 % of the total volumetric erosion measured across the whole watershed over the same period. Substantial deposition also took place in this area (1.195×10^5 [m^3]), which represents 54 % of the total volumetric deposition measured across the watershed over the period 2016-2020. Thus, erosion remains largely dominant (81%) with respect to deposition, and 3.783×10^5 [m^3] of material are exported, confirming the likely primary sources of coarse material during bedload transport events such as the one monitored on August 3rd, 2020.

Over the diffusive alluvial fan surfaces at the gully ends (zone 'ii' in Figure 12 and Table 1), morphological change tends to be dominated by deposition (92 % of total volume change). Patches of deposition with substantial depths (i.e. meters) notably occurred downstream of S17, downstream of S22, and to a lower extent downstream of S16. Another zone of deposition is visible on the alluvial fan downsteam of S11, at the confluence with the AdN main channel close to S10. Other depositional zones in similar settings (i.e. over the surface of alluvial fans, or at their feet close to the confluence with the AdN main channel) are visible downstream of S9, S6 and S4. About 36 % of the deposition measured over the whole watershed occurs in this alluvial fan dominated zone. In contrast, erosion is negligible (1.4 % of the erosion measured over the whole watershed), and a net deposition of 0.723×10^5 m^3 is measured in this zone over the period 2016-2020.

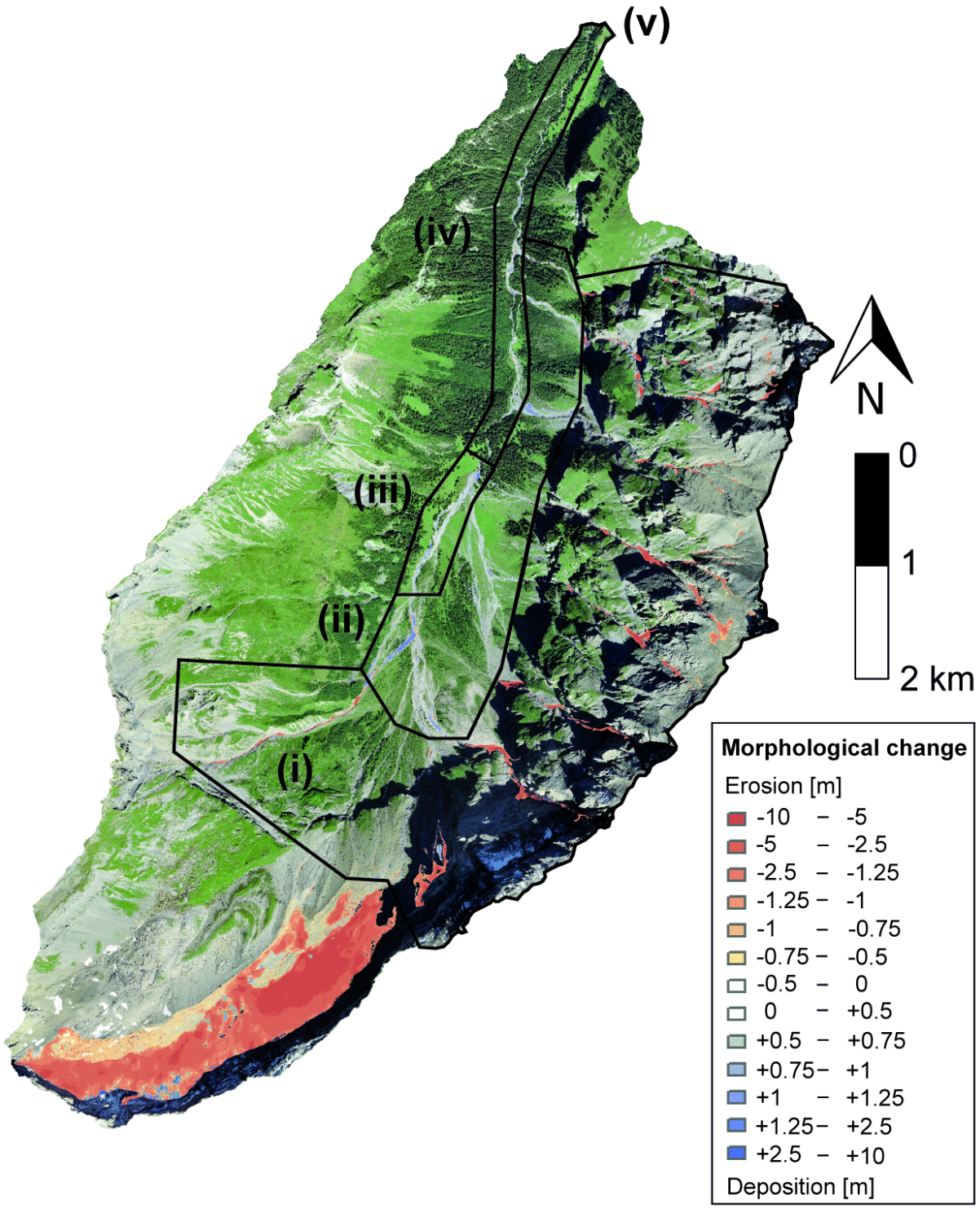
(v)
(iv)
(iii)
(ii)
(i)
N
0
1
2 km
Morphological change
Erosion [m]
-10 – -5
-5 – -2.5
-2.5 – -1.25
-1.25 – -1
-1 – -0.75
-0.75 – -0.5
-0.5 – 0
0 – +0.5
+0.5 – +0.75
+0.75 – +1
+1 – +1.25
+1.25 – +2.5
+2.5 – +10
Deposition [m]

Figure 12. Morphological change (erosion and deposition) measured through DEM differencing between two 0.5-m LIDAR-based SwissAlti3d models of 2016 and 2020, over an orthophoto 2020. Acknowledgments ©Swisstopo.

Along the braided channel section (zone 'iii' in Figure 12 and Table 1), deposition is also largely dominant with respect to erosion (91 %), notably around S14, S12 and S10; and 5.5 % of the deposition measured across the whole watershed takes place in this zone. Erosion is again negligible (0.2 % of the erosion measured over the whole watershed), and a net deposition of 0.109×10^5 [m^3] is measured in it over the period 2016-2020. Many areas of the braided channel zone 'iii' also present changeless surfaces. Along the semi-alluvial section (zone 'iv' in Figure 12 and Table 1), morphological changes tend to alternate between shallow patches of both erosion and deposition, with many areas also presenting changeless surfaces. Deposition again dominates the sediment budget (81%), and a net deposition of 0.074×10^5 [m^3] is measured, but both erosion and deposition volumes measured in zone 'iv' represent relatively small proportions with regards to the ones measured over the whole watershed (0.4 and 4.5 %, respectively). Over the whole watershed (v), erosion dominates the sediment budget (70 %), with a net export of 2.878×10^5 m^3.

Table 1. Erosion and deposition volumes measured through DEM differencing over the period 2016-2020 (numbers associated to Figure 12).

Zone	**Erosion (volume, percen.)**	**Deposition (volume, percen.)**	**Percen. Ero. vs Dep.**	**Net balance [$\times$ 10^5 m^3]**
(i) Tributaries	[$\times$ 10^5 m^3] 98 %	+1.195 [$\times$ 10^5 m^3] 54 %	%	
(ii) Alluvial fans	[$\times$ 10^5 m^3] 1.4 %	+0.797 [$\times$ 10^5 m^3] 36 %	%	+0.723
(iii) Braided section	[$\times$ 10^5 m^3] 0.2 %	+0.120 [$\times$ 10^5 m^3] 5.5 %	%	+0.109
(iv) Semi-alluvial section	[$\times$ 10^5 m^3] 0.4 %	+0.097 [$\times$ 10^5 m^3] 4.5 %	%	+0.074
(v) Whole watershed	[$\times$ 10^5 m^3] 100 %	+2.209 [$\times$ 10^5 m^3] 100 %	%	

4. Discussions

4.1 Evaluation of the seismic inversion approach

The two major bedload waves sensed by the SPG monitoring system (Figure 4) were both detected in the seismic-inverted time-series (Figure 6). Over the duration of the investigated bedload transport event, the instantaneous transport rates [$kg \cdot min^{-1}$] from the seismic monitoring tended to be higher, on average by a factor of 4, than the bedload transport rates measured with the SPG system for transport rates greater than 60 $kg \cdot min^{-1}$ (1 $kg \cdot s^{-1}$). The difference was lower for the peaks of the two major bedload waves identified in Figure 6 (factor 2.7 of difference). This result is positive and gives confidence to the validity of the FMI since all required parameters were determine beforehand in the field, the inversion was constrained without using measured data, and time-series were not scaled.

A range of reasons can be invoked to explain the residual difference between the SPG and the seismic-inverted time-series. It may be related to poor seismic inversion performance on the one hand. First, uncertainty in seismic inversion of bedload fluxes has been shown to arise in FMI from frequency overlaps between the bedload transport signal and the turbulence signal (Gimbert et al., 2014, 2019; Dietze et al., 2019; Bakker et al., 2020; Dietze et al., 2022). The presence of a waterfall (~1 m high) at the SPG weir (Figure 2a) may generate turbulence that contaminates the bedload-specific frequency bands used in the FMI (Schmandt et al., 2017), and may lead to overestimation of the inverted bedload transport rates. This observation aside, we were able to identify peaks in bedload transport rates synchronous with peaks measured with the SPG system, independently from peaks in water depths (as a proxy of turbulence rate; Figure 6), giving confidence in the capacity of the FMI to correctly partition between turbulence and bedload transport seismic signal. Water depth is easily measurable using stage sensors (Antoniazza et al., 2022; Nicollier et al., 2022) or pressure sensors (Dell'Agnese et al., 2015; Comiti et al., 2019). Further research should investigate how much improvement in the seismic inversion of bedload transport is achievable if exact measurements of water depths are used to drive the inversion. Seismic noise induced by rainfall drops may also overlap with bedload-specific frequency bands (Bakker et al., 2022) and contaminate the inversion of transport rates. This may be an explanation for the earlier onset of bedload transport inverted from the FMI as compared to the SPG recording, with strong seismic power recorded into high frequencies (> 45 Hz) in Figure 6 between 10:00 and 11:00.

Second, field estimates of the nine parameters needed to constrain FMI are also subject to uncertainty. Dietze et al. (2022) ran Monte Carlo simulations using random combinations of the nine parameters of the FMI picked within their own plausible range, and showed that inverted transport rates varied considerably (within an order of magnitude) between the different simulations. The model was shown to be particularly sensitive to grain-size parameterization (Gimbert et al., 2019; Bakker et al., 2020; Lagarde et al., 2021). In addition, the nine parameters were estimated during low flow conditions, while some of them (e.g. width, grain-size) may be changing through time, notably during flood flow conditions (Gimbert et al., 2019; Bakker et al., 2020; Dietze et al., 2022). In this

case, the section was relatively channelized making grain-size the likely cause of most uncertainty, but it emphasizes the need for accurate and representative field measurement of the FMI parameters, and further research may help to constraint the best approach to constraint each of them.

Part of the difference between the SPG and the seismic recording of bedload transport may be due to errors in the SPG recording on the other hand. The fact that over the event duration the total bedload transport mass measured with the SPG system was 74 % smaller than that inverted seismically could also reflect the higher particle detection threshold (> 10-20 mm) of the SPG system (Wyss et al., 2016; Nicollier et al., 2021b; Antoniazza et al., 2022). Smaller particles (1-10 mm) also emit seismic noise and are likely detected by seismometers, although the Tsai et al. (2012) model assumes the coarsest fractions ($> D_{90}$) to dominate the seismic signal (Lagarde et al., 2021). The difference in particle size detection threshold may nevertheless partly explain the greater mass of bedload transport seismic-inverted. Directly-sampled data for this station (Antoniazza et al., 2022) showed that 20 – 36 % of the sample mass was on average composed of particles that were smaller than the threshold of detection of the SPG system. This interpretation may be further supported by the earlier onset of bedload transport detected by seismic inversion (Figure 6; 10:00-11:00), if the onset of transport is size selective and small particles start moving first (Powell et al., 2001; Vericat et al., 2008). It is also possible that at very high transport rates the plates in the SPG are over-passed by some particle sizes (Rickenmann et al., 2012, 2014b), or the signal is saturated by simultaneous particle impacts (Coviello et al., 2022), which may also underestimate the transport rate.

That said, the difference is comparatively lower than that reported by Lagarde et al. (2021), and similar to that reported by Bakker et al. (2020), where seismic inversions of bedload transport were also compared with an independent measurement of bedload transport. Lagarde et al. (2021) compared their record with a Reid-type slot-sampler, using a similar seismic inversion approach to that applied here. They found differences in transport rate patterns as well as magnitudes with an average difference factor of 100 between instantaneous measures using the two methods. Their results likely reflected the grain-size limit of the slot-sampler (0.11 m), which may have inhibited the collection of the coarsest particles in transport (Lagarde et al. (2021), while the latter ($> D_{90}$) are again assumed to be responsible for the largest proportion of the seismic signal recorded (Tsai et al., 2012). Bakker et al. (2020) used an Elwha pressure-difference sampler as their benchmark data, and followed a similar seismic inversion approach to the one applied in this study. They reported a difference between the two monitoring systems within a factor of five, although the benchmark data were discrete in time, and not continuous as they are in this study. The good fit between the seismic-inverted bedload flux and the independent SPG monitoring (Figure 6), in both relative and absolute terms, provides confidence in the seismic inversion approach followed in this contribution. In addition, the relative coherence in the inverted bedload transport time-series

between spatially-consecutive seismic sensors and within individual tributaries (Figure 7, 8 and 9) gives further support with respect to the seismic inversion approach and in the derived bedload transport time-series. We emphasize that while uncertainties remain, the fact that we can readily generate bedload transport estimates across a watershed within an event illustrates the potential for seismic monitoring to unpack the anatomy of a bedload transport event.

4.2 Bedload transport event anatomy

The spatially-distributed absolute time-series of bedload transport (Figure 7, Figure 8, Figure 9) allow a number of observations with respect to the anatomy of a high-magnitude bedload transport event in a steep Alpine watershed.

4.2.1 Coarse material production in headwater tributaries

The observed bedload transport time-series showed that during such an event, it is not necessary to have hillslope-wide mobilization of material sources. Some torrents dominated supply material during the studied event (i.e. S4, S6, S11, S20, S21 and S22, notably), and others had very low transport rates (i.e. S9, S15 and S19). The most active torrents were not spatially contiguous even over what is a relatively small spatial area (maximum distance between any two tributary sensors is 2.5 km). Local tributary characteristics in terms of sediment availability may explain these differences, as well as local rainfall patterns (Michelon et al., 2021). Transported bedload in the headwater tributaries being a factor 2-3 greater than in the AdN main channel suggests that some of it was transported as debris floods or debris flows (Rickenmann and Koschni, 2010). This assertion can be tested by a simple calculation of the ratio between the mean bedload volume V_s [m^3] and the mean runoff volume V_w [m^3] in the main channel (MC) and torrential tributaries (TT), respectively. From Figure 4, we can estimate a mean water level of 0.19 m at the outlet monitoring station, which translates into a mean streamflow of 1.34 [$m^3 \cdot s^{-1}$] (Ceperley et al., 2018). Integrated over the duration of the event (11 hours), it means $V_w = 5.3 \times 10^4$ m^3. Scaling the outlet (13.4 km^2) runoff volume by the mean contributing area of main channel (9.82 km^2) and tributaries where bedload transport occurred (0.66 km^2), $V_{w\_MC} = 3.9 \times 10^4$ m^3 and $V_{w\_TT} = 0.26 \times 10^4$ m^3. The mean bedload volume is $V_{s\_MC} = 181$ m^3 in the main channel, and $V_{s\_TT} = 462$ m^3 in the tributaries. This translates into a ratio of bedload volume V_s over runoff volume V_w of 0.005 in the main channel, and of 0.18 in the tributaries. The difference is greater than an order of magnitude, and is in line with the partitioning between fluvial bedload transport and debris flow transport observed by Rickenmann and Koschni (2010). It confirms that coarse material in the tributaries was – at least partly – transported as debris floods or debris flows during the studied event, while fluvial bedload transport was dominant in the main channel.

4.2.2 Attenuation in the transported bedload through the watershed

The dataset shows how the basin itself rapidly attenuates (i.e. deposition occurs) the signal of hillslope erosion (Jerolmack and Paola, 2010; Ganti et al., 2014), in

this case primarily due to the presence of diffusive and therefore hydraulically less-efficient alluvial fans (e.g. downstream from S11) and braided sections (e.g. downstream of S16 and S17). Even large tributary inputs that would reach the main AdN channel are rapidly deposited to some extent (e.g. S6 tributary inputs to the main channel at S5 were largely attenuated by S3). These observations emphasize that attenuation of bedload transport is substantial for the studied high-magnitude bedload transport event, and that only a comparatively smaller proportion of the material mobilized in the watershed during the event is exported to the outlet (2.5 %). This is notably a consequence of the profile of formerly-glaciated landscapes, where the 'staircase' succession of steeper (e.g. rockwalls, rockslopes, riegls) and flatter (glacier troughs) sections significantly impact hydraulic efficiency (Hooke, 1991; Cook and Swift, 2012; Dell'Agnese et al., 2015; Lane et al., 2017; Antoniazza and Lane, 2021). There are few field data against which the present results can be compared, but the latter are in line with numerical simulations of coarse material transport in Alpine rivers, where large inputs from steep headwater tributaries were also rapidly deposited when reaching the flatter hydraulically less-efficient main channel network (Ferguson et al., 2006; Rickenmann et al., 2014a).

The attenuation of the bedload transport signal from headwater tributaries towards the outlet is also visible in the negative power law relationship between contributing area and the mass of bedload transported over the duration of the event (Figure 10e). It confirms a declining bedload transport Sediment Delivery Ratio (SDR) with distance downstream which was as yet only quantified in natural settings for the suspended load (Brown, 1949; Wu et al., 2018). As implied above, a primary driver of this decline is the transition from tributaries to the main river (compare the points on Figure 10e) and a transition from debris flow to fluvial bedload transport (Rickenmann and Koschni, 2010). The rate of attenuation is the greatest throughout the braided Section 3 (down to S10), while the bedload transport magnitude presents less variability through the mixed semi-alluvial and alluvial Section 4 (Figure 7, Figure 8, Figure 9). This relative constancy of the bedload transport magnitude through what is a quite long river reach (~2.8 km) is encouraging with regards to the development of 'Early Warning systems' for bedload transport events (Badoux et al., 2012; Chmiel et al., 2021).

4.2.3 Propagation of the bedload transporting event

From Figure 11, we identified that the bedload transport event first started in sub-catchment (d) and was later fed by sub-catchment (e) and (f), with relatively more material mobilized in (f). The analysis further emphasized the importance of tributary inputs for the timing and downstream propagation of the bedload transporting event, with bedload transport supply from some tributaries (e.g. S11, S6, S4) occurring sometimes earlier than the bedload wave moving through the main AdN channel (Figure 11a). Analysis of inter-sensor propagation velocities (Figure 11b) showed a substantial variability, but tended to be greater in steep tributaries (e.g. S11 10, S19 S17, S20 S16, S22 S18) than within flatter

sections of the main channel (e.g. S2 S1, S8 S7, S10 S8, S12 S10). Nevertheless, evidence of almost simultaneous bedload transport onset over sensors located multiple hundreds of meters away (e.g. S12 S14, S13 S16, S14 S17, S14 S18) questions the extent to which the same bedload material travels through the watershed and is sensed by multiple sensors, or whether we are rather facing a water wave that travels faster and (re-)mobilizes local material.

Typical values of bedload particle step-lengths and velocities measured within Alpine watersheds during individual flooding events may give insights in this question. Vázquez-Tarrío et al. (2019) reviewed particle tracking experiments and compiled results from 217 episodes of bedload particle transport measured in 30 gravel-bed rivers, during floods of varying magnitude (dimensionless stream power from 1.5^{-2} to 1.5^{0} [-]), and along reaches with contrasting gradient (i.e. 0.1 to 15 %) and morphologies (i.e. riffle-pool, step-pool, plane-bed, multithread). Mean particle travel distance during individual floods ranged from a few meters to a few hundred meters, mostly less than 200 meters (83% of events). Our seismic sensors were spaced from 268 to 882 meters, which makes it generally unlikely that the same bulk bedload transport was sensed over consecutive sensors, although the review by Vázquez-Tarrío et al. (2019) does not contain mean particle transport distances associated to debris-flow events, which may be greater (Coviello et al., 2019; Chmiel et al., 2021; Schimmel et al., 2022).

Mao et al. (2017) derived virtual bedload particle velocities (i.e. because of the possibility of resting periods in-between detections) between 10^{-5} and 35 $\mathrm{m \cdot min^{-1}}$ along a 13%-slope reach (plane-bed and step-pool morphology) of a glacier-fed river. Along a 4%-slope pool-riffle and step-pool river reach, Olinde and Johnson (2015) measured average particle step-lengths of 12.4 m and average transport duration of 0.5 min, which translated into an average velocity of ~24 $\mathrm{m \cdot min^{-1}}$, but particle steps were interspersed by resting periods that could last up to 190 hours. Much higher velocities were reported for debris-flow events: between 180 and 600 $\mathrm{m \cdot min^{-1}}$ in Schimmel et al. (2022), between 60 to 420 $\mathrm{m \cdot min^{-1}}$ in Chmiel et al. (2021), and between 84 and 300 $\mathrm{m \cdot min^{-1}}$ in Coviello et al. (2019). In this study, propagation velocities derived from consecutive seismic sensors ranged from 7 $\mathrm{m \cdot min^{-1}}$ up to ~100 $\mathrm{m \cdot min^{-1}}$, outside of the previously identified sensor pairs where bedload transport was almost simultaneous.

It is well-known that bedload transport is an intermittent process, characterized by periods particle of motion interspersed by periods of rest, both following an exponential distribution with thin-tails (i.e. the bulk bedload moving roughly homogeneously; Einstein, 1937; Ganti et al., 2010; Hassan et al., 2013; Ganti et al., 2014), although heavy-tailed super-diffusive distribution (i.e. few frontrunners being transported over larger distances than the bulk) have also been reported, typically over short durations (i.e. the flood scale; Liébault et al., 2012; Hassan et al., 2013; Phillips et al., 2013). The relatively long distance between the seismic sensors deployed in the frame of this study (268 to 882 meters), as well as the relatively high propagation velocities derived from the

cross-correlation analysis (7 $m \cdot min^{-1}$ up to ~100 $m \cdot min^{-1}$), makes it quite unlikely that the same bulk bedload transport is actually able to travel at such pace throughout the watershed.

The slower velocities derived from the cross-correlation analysis (Figure 11b) fall within the same range as the higher velocities found in particle tracking experiments (Mao et al., 2017; Olinde and Johnson, 2015), which means that some frontrunner particles may have been transported over longer distances (Hassan et al., 2013) and were consecutively measured by multiple seismic sensors. Yet, it is more likely that the bulk bedload transport travels more slowly, and therefore that derived velocities correspond to the propagation of a water wave, which (re-)mobilizes locally coarse material that is then transported over shorter distances. Using seismic networks, Cook et al. (2018) estimated the water wave of a GLOF to travel at velocities between 300 and 540 $m \cdot min^{-1}$, and Chmiel et al. (2022) reported velocities of a flash-flood in France between 300 and 360 $m \cdot min^{-1}$. The faster propagation velocities we derived from cross-correlation analysis (e.g. S12 S14, S13 S16, S14 S17, S14 S18) are not out-of-bounds with regards to the propagation velocity of other water waves reported in the literature. The fact that the tributaries have involved debris-flows may counter the argument that bedload is locally mobilized by a faster water wave. Indeed, greater velocities have been reported in the literature for this specific process (Chmiel et al., 2021; Coviello et al., 2019; Schimmel et al., 2022); and these are within the same range as those derived for the tributaries from the cross-correlation analysis (e.g. S11 10, S19 S17, S20 S16).

Previous hydrological research in the Vallon de Nant Alpine watershed has shown, through combined piezometer network, thermal imaging using an uncrewed airborne vehicle, isotope analysis and hydrological modelling (Michelon et al., 2022; Thornton et al., 2022), that substantial groundwater release takes place throughout Section 3 (Figure 1), where almost simultaneous bedload transport waves were measured in some instances between sensors spaced hundreds of meters away (e.g. S12 S14, S14 S17). Local hydrological conditions (e.g. notably associated with vertical hyporheic fluxes) may locally reduce the critical shear stress required for entrainment, and may increase sediment mobilization and transport capacity independently from the downstream propagation of the water wave, translating into simultaneous bedload transport mobilized at different locations of the watershed. The effect of groundwater release on coarse material mobilization deserves more attention in future research. Valuable knowledge of the respective propagation of water waves and bedload waves through Alpine watersheds may be gained from the deployment of distributed acoustic sensors (DAS), km-long fiber optic cables able to deliver seismic data almost continuously in space and time (Zhan, 2019; Lior et al., 2021).

4.3 Longer-term perspectives on watershed-scale sedimentary fluxes

The seismic sensor network deployed in the frame of this study revealed the anatomy of a high-magnitude bedload transport event in terms of coarse material production in headwater tributaries, bedload transport attenuation through-

out the watershed and event timing and propagation velocity. We now place these observations in a longer perspective of coarse material flux throughout Alpine watersheds with the help of the morphological change analysis.

During the studied event – with the 5th greatest bedload transport peak of the period 2016-2020 – the proportion of coarse material exported at the outlet was negligible (2.5%) compared to that mobilized throughout the watershed, and notably in headwater tributaries, which means that substantial deposition took place within the main channel network. Supply exceeded capacity and the event was deposition-dominated (Turowski et al., 2013). If such events were the rule, it would mean the main channel network would be aggrading on the longer term. This assertion can be confronted to a set of summary statements made from the morphological change analysis. First, 76 % of the material volume mobilized in the headwater tributaries are exported at the outlet over the period 2016-2020, which is substantially more than the proportion measured during the 3rd of August flood (2.5 %). This means that we do not observe on longer term the general aggradation of the channel network we would see if the substantial deposition measured during the 3rd of August event was the rule in terms of bedload transport event dynamics. Instead, material mobilized in headwater tributaries and deposited within the main channel network during high-magnitude events such as the one that occurs on August 3rd 2020 is likely then progressively evacuated by subsequent competent flows. Those empirical data are in line with the 'graded channel theory' of Mackin (1948) and (Lane, 1955), where streams adjust on the longer term their gradient by producing erosion and deposition to evacuate material supplied from upstream. As reported as a characteristic of hillslope to river sediment transport coupling (Newson, 1980), lower competent flows than that reported here for the 3rd August 2020 may be more geomorphically effective because of the sediment delivered, but not evacuated during the August 2020 event.

Second, results of the morphological change analysis show that a greater proportion of material exported from headwater tributaries is stored within alluvial fans (19 %) over the period 2016-2020, than within the braided section (3 %) and the semi-alluvial section (2 %). During the 3rd of August 2020 event, a considerable attenuation in transported bedload was also observed within the braided river reach (Figure 8, Figure 9). This means that in the longer term, material deposited within alluvial braided channel during high-magnitude events may be more easily reworked and exported during subsequent competent flows (Mackin, 1948; Lane, 1955) than the one deposited over the diffusive surface of alluvial fans.

Third, the fact that 98 % of the erosion takes place in the headwater tributary zone, and that little erosion proportionally occurs in the other morphological units (e.g. alluvial fans, braided channels, semi-alluvial channels) tends to confirm the view of Piton and Recking (2017) on the importance of 'travelling bedload'. Bedload produced in distal headwater tributary sources seems to be transported in the main channel network without inducing in proportion ma-

jor (re)mobilization, in particular along alluvial fans and semi-alluvial reaches. The latter play a role of storage or conveyor, rather than a sedimentary source. This trend was clear in the semi-alluvial section during the 3rd of August event, where the bedload transport magnitude was held relatively constant through a substantial length of channel (~2.8 km; Figure 8, Figure 9). This behaviour can be related to the concept of 'washload' developed for the suspended load, consisting of particles found in the water column with sizes finer than the ones composing the bed (Vanoni, 2006; Turowski et al., 2010; Piton and Recking, 2017), mobilized in distal sources and conveyed through a main channel network that experiences little erosion or deposition.

High-magnitude events in the tributaries such as the one that occurred on August, 3rd 2020 may thus likely play an important role with regards to longer term coarse material fluxes by providing material into the main channel network from areas of the watershed where large sedimentary sources are available (e.g. steep slopes at the top of rockwalls, tributary gullies, the glacier area), but which may not always be well connected during low to intermediate flows (Cavalli et al., 2013; Lane et al., 2017; Comiti et al., 2019; Buter et al., 2022). By supplying material into the main channel network, high-magnitude events in the tributaries may therefore supply new material which will on the longer term be remobilized during subsequent low, intermediate and high magnitude events in the main channel network (Cavalli et al., 2013; Turowski et al., 2013; Lane et al., 2017), balancing the sediment budget towards the 'grade' on the longer term (Mackin, 1948; Lane, 1955).

The morphological change analysis shows a net sediment export of 2.878×10^5 m^3 over the period 2016-2020. By computing bedload export from the SPG measurement over the exact same period (August 25th 2016 to August 6th 2020), 0.025×10^5 m^3 are derived, that is about 1%. This would mean that 99% of the total volumetric sediment exported from the Vallon de Nant Alpine watershed is composed of material not detected by the SPG system. A large proportion of it is likely transported through suspension, which can represent $> 90\%$ of Alpine watershed sedimentary budget (Turowski et al., 2010; Hinderer et al., 2013). Some fraction of it may also be due to bedload particles missed by the SPG system, typically if they are smaller than the size detection threshold of 10-20 mm (Nicollier et al., 2022), if saturation occurs at high bedload transport rates (Coviello et al., 2022), or if particle hops are greater than the SPG streamwise length when turbulence rate is higher (Schneider et al., 2014; Rickenmann et al., 2014b). But errors in the volumetric erosion and deposition may also arise from the DEMs used in the morphological change analysis (Lindsay and Ashmore, 2002; Bater and Coops, 2009; Wheaton et al., 2010).

5. Conclusion

The way Alpine watersheds mobilize, convey and store coarse material is poorly constrained, which limits the accuracy of current bedload transport predictions. Environmental seismology applied to Alpine rivers, and combined with appropriate seismic physical models, provides absolute time-series of bedload trans-

port, with an average factor 4 of difference in this study when compared to an independent calibrated time-series of bedload transport. Distributed seismic networks have the potential for tracking the motion of coarse material through Alpine watersheds and may help to constraint better and to improve prediction of bedload transport fluxes in the future.

The 24 seismic sensors deployed during this study, and the spatially-distributed time-series of bedload transport derived from them, have shown the relative inefficiency of the Vallon de Nant Alpine watershed in evacuating coarse material, even during what is a relatively infrequent high-magnitude bedload transport event. Large inputs measured in some of the tributaries, likely transported at least partly as debris-floods or debris flows, were indeed rapidly attenuated as the flow was crossing less hydraulically-efficient reaches, and only a comparatively negligible proportion of the total amount of material mobilized in the headwater tributaries is actually exported at the outlet. Not every tributary transported bedload during the studied event, even at this small spatial scale, which underlines the importance of local sediment availability. Cross-correlation analysis of the time-series suggested that a faster water wave was (re-)mobilizing local material, and coarse sediment was expected to move slower, and over shorter distances. Multiple periods of competent flows are necessary to evacuate the coarse material mobilized throughout the watershed during the studied event. High-magnitude bedload transport events in the tributaries nevertheless appeared to be important to supply new material in the main channel network from poorly-connected sourcing areas of the watershed, which are on the longer term progressively evacuated from it by subsequent competent flows.

Conflict of Interest

The authors declare no conflicts of interest relevant to this study.

Data availability statement

The data presented in this study will be made available online on the EnviDat repository https://www.envidat.ch/dataset/sediment-transport-observations-in-swiss-mountain-streams upon publication of the manuscript.

Acknowledgments

The authors thank the University of Lausanne and the Swiss National Science Foundation SNSF (Grant P1LAP2_194974 awarded to GA) for supporting this work. The University of Lausanne, the Swiss Federal Research Institute WSL, and the Physics of Environmental Systems group of the ETH Zürich are further thanked for financing the building of the SPG monitoring station at the Vallon de Nant. The Faculty of Geosciences and Environment of the University of Lausanne funded the acquisition of field equipment. The Geomorphology Section 4.6 at the GFZ Potsdam is thanked for hosting GA during his Doc.Mobility project, and for the support and expertise provided with environmental seismology data processing. The Geophysical Instrument Pool Potsdam (GIPP) of the GFZ provided seismic instruments (grant number GIPP202006-RAAC II).

The authors are grateful to Magalí Matteodo, Mehdi Mattou, Floreana Miesen, Aurélien Ballu, Nora Krebs, Sabrina Hennig, François Bonnet, Valentin Quartenoud and family, Sylvain Bernard and family, and the team at 'Auberge de Pont de Nant', for their support in the field.

6. References

Antoniazza, G., Bakker, M., Lane, S.N., 2019. Revisiting the morphological method in two-dimensions to quantify bed-material transport in braided rivers. Earth Surface Processes and Landforms 44, 2251–2267. https://doi.org/10.1002/esp.4633Antoniazza, G., Lane, S.N., 2021. Sediment yield over glacial cycles: A conceptual model. Progress in Physical Geography: Earth and Environment 0309133321997292. https://doi.org/10.1177/0309133321997292Antoniazza, G., Nicollier, T., Boss, S., Mettra, F., Badoux, A., Schaefli, B., Rickenmann, D., Lane, S.N., 2022. Hydrological Drivers of Bedload Transport in an Alpine Watershed. Water Resources Research 58, e2021WR030663. https://doi.org/10.1029/2021WR030663Antoniazza, G., Nicollier, T., Wyss, C.R., Boss, S., Rickenmann, D., 2020. Bedload Transport Monitoring in Alpine Rivers: Variability in Swiss Plate Geophone Response. Sensors 20, 4089. https://doi.org/10.3390/s20154089Badoux, A., Andres, N., Techel, F., Hegg, C., 2016. Natural hazard fatalities in Switzerland from 1946 to 2015. Natural Hazards and Earth System Sciences 16, 2747–2768.Badoux, A., Andres, N., Turowski, J., 2014. Damage costs due to bedload transport processes in Switzerland. Natural Hazards and Earth System Sciences 14, 279–294. https://doi.org/10.5194/nhess-14-279-2014Badoux, A., Turowski, J.M., Mao, L., Mathys, N., Rickenmann, D., 2012. Rainfall intensity–duration thresholds for bedload transport initiation in small Alpine watersheds. Natural Hazards and Earth System Sciences 12, 3091–3108. https://doi.org/10.5194/nhess-12-3091-2012Badoux, H., 1971. Feuille 1305 Dent de Morcles.Bakker, M., Antoniazza, G., Odermatt, E., Lane, S.N., 2019. Morphological Response of an Alpine Braided Reach to Sediment-Laden Flow Events. Journal of Geophysical Research: Earth Surface 124, 1310–1328. https://doi.org/10.1029/2018JF004811Bakker, M., Gimbert, F., Geay, T., Misset, C., Zanker, S., Recking, A., 2020. Field Application and Validation of a Seismic Bedload Transport Model. Journal of Geophysical Research: Earth Surface 125, e2019JF005416. https://doi.org/10.1029/2019JF005416Bakker, M., Legout, C., Gimbert, F., Nord, G., Boudevillain, B., Freche, G., 2022. Seismic modelling and observations of rainfall. Journal of Hydrology 610, 127812. https://doi.org/10.1016/j.jhydrol.2022.127812Bater, C.W., Coops, N.C., 2009. Evaluating error associated with lidar-derived DEM interpolation. Computers & Geosciences 35, 289–300. https://doi.org/10.1016/j.cageo.2008.09.001Brown, C.B., 1949. Sediment transportation, in: House, R. Engineering Hydraulics. New-York, pp. 769–857.Burtin, A., Cattin, R., Bollinger, L., Vergne, J., Steer, P., Robert, A., Findling, N., Tiberi, C., 2011. Towards the hydrologic and bed load monitoring from high-frequency seismic noise in a braided river: The "torrent de St Pierre", French Alps. Journal of hydrology 408, 43–53.Buter, A., Heckmann, T., Filisetti, L., Savi, S., Mao, L., Gems, B.,

Comiti, F., 2022. Effects of catchment characteristics and hydro-meteorological scenarios on sediment connectivity in glacierised catchments. Geomorphology 402, 108128. https://doi.org/10.1016/j.geomorph.2022.108128Cavalli, M., Trevisani, S., Comiti, F., Marchi, L., 2013. Geomorphometric assessment of spatial sediment connectivity in small Alpine catchments. Geomorphology, Sediment sources, source-to-sink fluxes and sedimentary budgets 188, 31–41. https://doi.org/10.1016/j.geomorph.2012.05.007Ceperley, N., Michelon, A., Escoffier, N., Mayoraz, G., Boix Canadell, M., Horgby, A., Hammer, F., Antoniazza, G., Schaefli, B., Lane, S., Rickenmann, D., Boss, S., 2018. Salt Gauging And Stage-Discharge Curve, Avançon De Nant, Outlet Vallon De Nant Catchment. https://doi.org/10.5281/zenodo.1154798. Version V1.0.0 [Data set]. Zenodo.Ceperley, N., Zuecco, G., Beria, H., Carturan, L., Michelon, A., Penna, D., Larsen, J., Schaefli, B., 2020. Seasonal snow cover decreases young water fractions in high Alpine catchments. Hydrological Processes 34, 4794–4813. https://doi.org/10.1002/hyp.13937Chmiel, M., Godano, M., Piantini, M., Brigode, P., Gimbert, F., Bakker, M., Courboulex, F., Ampuero, J.-P., Rivet, D., Sladen, A., Ambrois, D., Chapuis, M., 2022. Brief communication: Seismological analysis of flood dynamics and hydrologically triggered earthquake swarms associated with Storm Alex. Natural Hazards and Earth System Sciences 22, 1541–1558. https://doi.org/10.5194/nhess-22-1541-2022Chmiel, M., Walter, F., Wenner, M., Zhang, Z., McArdell, B.W., Hibert, C., 2021. Machine Learning Improves Debris Flow Warning. Geophysical Research Letters 48, e2020GL090874. https://doi.org/10.1029/2020GL090874Comiti, F., Mao, L., Penna, D., Dell'Agnese, A., Engel, M., Rathburn, S., Cavalli, M., 2019. Glacier melt runoff controls bedload transport in Alpine catchments. Earth and Planetary Science Letters 520, 77–86. https://doi.org/10.1016/j.epsl.2019.05.031Cook, K.L., Andermann, C., Gimbert, F., Adhikari, B.R., Hovius, N., 2018. Glacial lake outburst floods as drivers of fluvial erosion in the Himalaya. Science 362, 53–57. https://doi.org/10.1126/science.aat4981Cook, K.L., Dietze, M., 2022. Seismic Advances in Process Geomorphology. Annual Review of Earth and Planetary Sciences 50, 183–204. https://doi.org/10.1146/annurev-earth-032320-085133Cook, S.J., Swift, D.A., 2012. Subglacial basins: Their origin and importance in glacial systems and landscapes. Earth-Science Reviews 115, 332–372. https://doi.org/10.1016/j.earscirev.2012.09.009Coviello, V., Arattano, M., Comiti, F., Macconi, P., Marchi, L., 2019. Seismic Characterization of Debris Flows: Insights into Energy Radiation and Implications for Warning. Journal of Geophysical Research: Earth Surface 124, 1440–1463. https://doi.org/10.1029/2018JF004683Coviello, V., Vignoli, G., Simoni, S., Bertoldi, W., Engel, M., Buter, A., Marchetti, G., Andreoli, A., Savi, S., Comiti, F., 2022. Bedload fluxes in a glacier-fed river at multiple temporal scales. Water Resources Research n/a, e2021WR031873. https://doi.org/10.1029/2021WR031873Dell'Agnese, A., Brardinoni, F., Toro, M., Mao, L., Engel, M., Comiti, F., 2015. Bedload transport in a formerly glaciated mountain catchment constrained by particle tracking. Earth Surface Dynamics 3, 527–542. https://doi.org/10.5194/esurf-3-527-2015Dietze, M.,

2018. The R package “eseis”–a software toolbox for environmental seismology. Earth Surface Dynamics 6, 669–686.Dietze, M., Bell, R., Ozturk, U., Cook, K.L., Andermann, C., Beer, A.R., Damm, B., Lucia, A., Fauer, F.S., Nissen, K.M., Sieg, T., Thieken, A.H., 2022. More than heavy rain turning into fast-flowing water – a landscape perspective on the 2021 Eifel floods. Natural Hazards and Earth System Sciences 22, 1845–1856. https://doi.org/10.5194/nhess-22-1845-2022Dietze, M., Lagarde, S., Halfi, E., Laronne, J., Turowski, J.M., 2019. Joint sensing of bedload flux and water depth by seismic data inversion. https://doi.org/10.31223/osf.io/n5gcmDowning, J., 2010. Acoustic gravel-momentum sensor. US Geological Survey Scientific Investigations Report 5091, 143–158.Dutoit, A., 1983. La végétation de l’étage subalpin du Vallon de Nant. Université de Lausanne. Lausanne.Egholm, D.L., Pedersen, V.K., Knudsen, M.F., Larsen, N.K., 2012. Coupling the flow of ice, water, and sediment in a glacial landscape evolution model. Geomorphology 141–142, 47–66. https://doi.org/10.1016/j.geomorph.2011.12.019Einstein, H.A., 1937. Bedload transport as a probability problem. Sedimentation 1027, C1–C105.Ferguson, R.I., Cudden, J.R., Hoey, T.B., Rice, S.P., 2006. River system discontinuities due to lateral inputs: generic styles and controls. Earth Surface Processes and Landforms 31, 1149–1166. https://doi.org/10.1002/esp.1309Ganti, V., Lamb, M.P., McElroy, B., 2014. Quantitative bounds on morphodynamics and implications for reading the sedimentary record. Nat Commun 5, 3298. https://doi.org/10.1038/ncomms4298Ganti, V., Meerschaert, M.M., Foufoula-Georgiou, E., Viparelli, E., Parker, G., 2010. Normal and anomalous diffusion of gravel tracer particles in rivers. Journal of Geophysical Research: Earth Surface 115. https://doi.org/10.1029/2008JF001222Gimbert, F., Fuller, B.M., Lamb, M.P., Tsai, V.C., Johnson, J.P.L., 2019. Particle transport mechanics and induced seismic noise in steep flume experiments with accelerometer-embedded tracers. Earth Surface Processes and Landforms 44, 219–241. https://doi.org/10.1002/esp.4495Gimbert, F., Tsai, V.C., Lamb, M.P., 2014. A physical model for seismic noise generation by turbulent flow in rivers. Journal of Geophysical Research: Earth Surface 119, 2209–2238. https://doi.org/10.1002/2014JF003201Gomez, B., Soar, P.J., 2022. Bedload transport: beyond intractability. Royal Society Open Science 9, 211932. https://doi.org/10.1098/rsos.211932Hassan, M.A., Voepel, H., Schumer, R., Parker, G., Fraccarollo, L., 2013. Displacement characteristics of coarse fluvial bed sediment. Journal of Geophysical Research: Earth Surface 118, 155–165.Hinderer, M., Kastowski, M., Kamelger, A., Bartolini, C., Schlunegger, F., 2013. River loads and modern denudation of the Alps — A review. Earth-Science Reviews 118, 11–44. https://doi.org/10.1016/j.earscirev.2013.01.001Hooke, R.L., 1991. Positive feedbacks associated with erosion of glacial cirques and overdeepenings. GSA Bulletin 103, 1104–1108. https://doi.org/10.1130/0016-7606(1991)103<1104:PFAWEO>2.3.CO;2Jerolmack, D.J., Paola, C., 2010. Shredding of environmental signals by sediment transport. Geophysical Research Letters 37. https://doi.org/10.1029/2010GL044638Kreisler, A., Moser, M., Aigner, J., Rindler, R., Tritthart, M., Habersack, H., 2017.

Analysis and classification of bedload transport events with variable process characteristics. Geomorphology, SEDIMENT DYNAMICS IN ALPINE BASINS 291, 57–68. https://doi.org/10.1016/j.geomorph.2016.06.033Lagarde, S., Dietze, M., Gimbert, F., Laronne, J.B., Turowski, J.M., Halfi, E., 2021. Grain-Size Distribution and Propagation Effects on Seismic Signals Generated by Bedload Transport. Water Resources Research 57, e2020WR028700. https://doi.org/10.1029/2020WR028700Lane, E.W., 1955. Importance of fluvial morphology in hydraulic engineering. Proceedings (American Society of Civil Engineers); v. 81, paper no. 745.Lane, S.N., Bakker, M., Gabbud, C., Micheletti, N., Saugy, J.-N., 2017. Sediment export, transient landscape response and catchment-scale connectivity following rapid climate warming and Alpine glacier recession. Geomorphology, Connectivity in Geomorphology from Binghamton 2016 277, 210–227. https://doi.org/10.1016/j.geomorph.2016.02.015Lane, S.N., Borgeaud, L., Vittoz, P., 2016. Emergent geomorphic–vegetation interactions on a subalpine alluvial fan. Earth Surface Processes and Landforms 41, 72–86. https://doi.org/10.1002/esp.3833Liébault, F., Bellot, H., Chapuis, M., Klotz, S., Deschâtres, M., 2012. Bedload tracing in a high-sediment-load mountain stream. Earth Surface Processes and Landforms 37, 385–399. https://doi.org/10.1002/esp.2245Lindsay, J., Ashmore, P., 2002. The effects of survey frequency on estimates of scour and fill in braided river model. Earth Surface Processes and Landforms 27, 27–43. https://doi.org/10.1002/esp.282Lior, I., Sladen, A., Rivet, D., Ampuero, J.-P., Hello, Y., Becerril, C., Martins, H.F., Lamare, P., Jestin, C., Tsagkli, S., Markou, C., 2021. On the Detection Capabilities of Underwater Distributed Acoustic Sensing. Journal of Geophysical Research: Solid Earth 126, e2020JB020925. https://doi.org/10.1029/2020JB020925Mächler, E., Salyani, A., Walser, J.-C., Larsen, A., Schaefli, B., Altermatt, F., Ceperley, N., 2021. Environmental DNA simultaneously informs hydrological and biodiversity characterization of an Alpine catchment. Hydrology and Earth System Sciences 25, 735–753. https://doi.org/10.5194/hess-25-735-2021Mackin, H., 1948. CONCEPT OF THE GRADED RIVER. GSA Bulletin 59, 463–512. https://doi.org/10.1130/0016-7606(1948)59[463:COTGR]2.0.CO;2Mancini, D., Lane, S.N., 2020. Changes in sediment connectivity following glacial debuttressing in an Alpine valley system. Geomorphology 352, 106987. https://doi.org/10.1016/j.geomorph.2019.106987Mao, L., Dell'Agnese, A., Comiti, F., 2017. Sediment motion and velocity in a glacier-fed stream. Geomorphology 291, 69–79.Maurer, J.M., Schaefer, J.M., Russell, J.B., Rupper, S., Wangdi, N., Putnam, A.E., Young, N., 2020. Seismic observations, numerical modeling, and geomorphic analysis of a glacier lake outburst flood in the Himalayas. Science Advances 6, eaba3645. https://doi.org/10.1126/sciadv.aba3645MeteoSwiss, 2019. Daily Precipitation (final analysis): Rhires D. Documentation of MeteoSwiss, Grid-Data Products.MeteoSwiss, 2017. Daily Mean, Minimum and Maximum Temperature: TabsD, TminD, TmaxD. Documentation of MeteoSwiss Grid-Data Products.Michelon, A., Benoit, L., Beria, H., Ceperley, N., Schaefli, B., 2021.

Benefits from high-density rain gauge observations for hydrological response analysis in a small alpine catchment. Hydrology and Earth System Sciences 25, 2301–2325. https://doi.org/10.5194/hess-25-2301-2021Michelon, A., Ceperley, N., Beria, H., Larsen, J., Vennemann, T., Schaefli, B., 2022. Studying the dynamic of a high alpine catchment based on multiple natural tracers. Hydrology and Earth System Sciences Discussions 1–43. https://doi.org/10.5194/hess-2022-48Mizuyama, T., Laronne, J.B., Nonaka, M., Sawada, T., Satofuka, Y., Matsuoka, M., Yamashita, S., Sako, Y., Tamaki, S., Watari, M., 2010. Calibration of a passive acoustic bedload monitoring system in Japanese mountain rivers. US Geological Survey Scientific Investigations Report 5091, 296–318.Mueller, E.R., Pitlick, J., 2005. Morphologically based model of bed load transport capacity in a headwater stream. Journal of Geophysical Research: Earth Surface 110. https://doi.org/10.1029/2003JF000117Newson, M., 1980. The geomorphological effectiveness of floods—a contribution stimulated by two recent events in mid-wales. Earth Surface Processes 5, 1–16. https://doi.org/10.1002/esp.3760050102Nicollier, T., Antoniazza, G., Ammann, L., Rickenmann, D., Kirchner, J.W., 2022. Toward a general calibration of the Swiss plate geophone system for fractional bedload transport. Earth Surface Dynamics Discussions 1–29. https://doi.org/10.5194/esurf-2022-7Nicollier, T., Antoniazza, G., Rickenmann, D., Hartlieb, A., Kirchner, J.W., 2021a. Improving the Calibration of Impact Plate Bedload Monitoring Systems by Filtering Out Acoustic Signals from Extraneous Particle Impacts.Nicollier, T., Rickenmann, D., Hartlieb, A., 2021b. Field and flume measurements with the impact plate: effect of bedload grain-size distribution on signal response. Earth Surface Processes and Landforms n/a. https://doi.org/10.1002/esp.5117Olinde, L., Johnson, J.P.L., 2015. Using RFID and accelerometer-embedded tracers to measure probabilities of bed load transport, step lengths, and rest times in a mountain stream. Water Resources Research 51, 7572–7589. https://doi.org/10.1002/2014WR016120Phillips, C.B., Martin, R.L., Jerolmack, D.J., 2013. Impulse framework for unsteady flows reveals superdiffusive bed load transport. Geophysical Research Letters 40, 1328–1333. https://doi.org/10.1002/grl.50323Piantini, M., Gimbert, F., Bakker, M., Recking, A., Nanni, U., 2022. Using a dense seismic array to study fluvial processes in a braided river reach under flood conditions. LHB 0, 2053314. https://doi.org/10.1080/27678490.2022.2053314Piton, G., Recking, A., 2017. The concept of travelling bedload and its consequences for bedload computation in mountain streams. Earth Surface Processes and Landforms 42, 1505–1519. https://doi.org/10.1002/esp.4105Powell, D.M., Reid, I., Laronne, J.B., 2001. Evolution of bed load grain size distribution with increasing flow strength and the effect of flow duration on the caliber of bed load sediment yield in ephemeral gravel bed rivers. Water Resources Research 37, 1463–1474. https://doi.org/10.1029/2000WR900342Rainato, R., Mao, L., García-Rama, A., Picco, L., Cesca, M., Vianello, A., Preciso, E., Scussel, G.R., Lenzi, M.A., 2017. Three decades of monitoring in the Rio Cordon instrumented basin: Sediment budget and temporal trend of sediment yield. Geomorphology, SEDIMENT DYNAMICS IN ALPINE BASINS 291, 45–56.

https://doi.org/10.1016/j.geomorph.2016.03.012Rainato, R., Mao, L., Picco, L., 2018. Near-bankfull floods in an Alpine stream: Effects on the sediment mobility and bedload magnitude. International Journal of Sediment Research 33, 27–34. https://doi.org/10.1016/j.ijsrc.2017.03.006Recking, A., Leduc, P., Liébault, F., Church, M., 2012. A field investigation of the influence of sediment supply on step-pool morphology and stability. Geomorphology 139–140, 53–66. https://doi.org/10.1016/j.geomorph.2011.09.024Rickenmann, D., 2020. Effect of Sediment Supply on Cyclic Fluctuations of the Disequilibrium Ratio and Threshold Transport Discharge, Inferred From Bedload Transport Measurements Over 27 Years at the Swiss Erlenbach Stream. Water Resources Research 56, e2020WR027741. https://doi.org/10.1029/2020WR027741Rickenmann, D., 2018. Variability of Bed Load Transport During Six Summers of Continuous Measurements in Two Austrian Mountain Streams (Fischbach and Ruetz). Water Resources Research 54, 107–131. https://doi.org/10.1002/2017WR021376Rickenmann, D., 2017. Bedload transport measurements with geophones, hydrophones and underwater microphones (passive acoustic methods). Gravel Bed Rivers and Disasters, Wiley & Sons, Chichester, UK 185–208.Rickenmann, D., Heimann, F.U.M., Turowski, J.M., Bieler, C., Böckli, M., Badoux, A., 2014a. Simulation of bedload transport in the Hasliaare River with increased sediment input, in: River Flow. pp. 2273–2281.Rickenmann, D., Koschni, A., 2010. Sediment loads due to fluvial transport and debris flows during the 2005 flood events in Switzerland. Hydrological Processes: An International Journal 24, 993–1007.Rickenmann, D., Turowski, J.M., Fritschi, B., Klaiber, A., Ludwig, A., 2012. Bedload transport measurements at the Erlenbach stream with geophones and automated basket samplers. Earth Surface Processes and Landforms 37, 1000–1011.Rickenmann, D., Turowski, J.M., Fritschi, B., Wyss, C., Laronne, J., Barzilai, R., Reid, I., Kreisler, A., Aigner, J., Seitz, H., Habersack, H., 2014b. Bedload transport measurements with impact plate geophones: comparison of sensor calibration in different gravel-bed streams. Earth Surface Processes and Landforms 39, 928–942. https://doi.org/10.1002/esp.3499Roth, D.L., Brodsky, E.E., Finnegan, N.J., Rickenmann, D., Turowski, J.M., Badoux, A., 2016. Bed load sediment transport inferred from seismic signals near a river. Journal of Geophysical Research: Earth Surface 121, 725–747. https://doi.org/10.1002/2015JF003782Schimmel, A., Coviello, V., Comiti, F., 2022. Debris flow velocity and volume estimations based on seismic data. Natural Hazards and Earth System Sciences 22, 1955–1968. https://doi.org/10.5194/nhess-22-1955-2022Schmandt, B., Gaeuman, D., Stewart, R., Hansen, S.M., Tsai, V.C., Smith, J., 2017. Seismic array constraints on reach-scale bedload transport. Geology 45, 299–302.Schneider, J.M., Turowski, J.M., Rickenmann, D., Hegglin, R., Arrigo, S., Mao, L., Kirchner, J.W., 2014. Scaling relationships between bed load volumes, transport distances, and stream power in steep mountain channels. Journal of Geophysical Research: Earth Surface 119, 533–549. https://doi.org/10.1002/2013JF002874Thornton, J.M., Brauchli, T., Mariethoz, G., Brunner, P., 2021. Efficient multi-objective calibration and uncertainty analysis of distributed snow simulations in rugged alpine terrain. Journal of Hy-

drology 598, 126241. https://doi.org/10.1016/j.jhydrol.2021.126241Thornton, J.M., Mariethoz, G., Brunner, P., 2018. A 3D geological model of a structurally complex Alpine region as a basis for interdisciplinary research. Sci Data 5, 180238. https://doi.org/10.1038/sdata.2018.238Thornton, J.M., Therrien, R., Mariéthoz, G., Linde, N., Brunner, P., 2022. Simulating Fully-Integrated Hydrological Dynamics in Complex Alpine Headwaters: Potential and Challenges. Water Resources Research 58, e2020WR029390. https://doi.org/10.1029/2020WR029390Tsai, V.C., Minchew, B., Lamb, M.P., Ampuero, J.-P., 2012. A physical model for seismic noise generation from sediment transport in rivers. Geophysical Research Letters 39. https://doi.org/10.1029/2011GL050255Turowski, J.M., 2012. Semi-Alluvial Channels and Sediment-Flux-Driven Bedrock Erosion, in: Gravel-Bed Rivers. John Wiley & Sons, Ltd, pp. 399–418. https://doi.org/10.1002/9781119952497.ch29Turowski, J.M., Badoux, A., Leuzinger, J., Hegglin, R., 2013. Large floods, alluvial overprint, and bedrock erosion. Earth Surface Processes and Landforms 38, 947–958. https://doi.org/10.1002/esp.3341Turowski, J.M., Rickenmann, D., Dadson, S.J., 2010. The partitioning of the total sediment load of a river into suspended load and bedload: a review of empirical data. Sedimentology 57, 1126–1146. https://doi.org/10.1111/j.1365-3091.2009.01140.xTurowski, J.M., Yager, E.M., Badoux, A., Rickenmann, D., Molnar, P., 2009. The impact of exceptional events on erosion, bedload transport and channel stability in a step-pool channel. Earth Surface Processes and Landforms 34, 1661–1673. https://doi.org/10.1002/esp.1855Vanoni, V.A., 2006. Sedimentation Engineering. American Society of Civil Engineers. https://doi.org/10.1061/9780784408230Vázquez-Tarrío, D., Recking, A., Liébault, F., Tal, M., Menéndez-Duarte, R., 2019. Particle transport in gravel-bed rivers: Revisiting passive tracer data. Earth Surface Processes and Landforms 44, 112–128. https://doi.org/10.1002/esp.4484Vericat, D., Batalla, R.J., Gibbins, C.N., 2008. Sediment entrainment and depletion from patches of fine material in a gravel-bed river. Water Resources Research 44. https://doi.org/10.1029/2008WR007028Vittoz, P., Gmür, P., 2009. Introduction aux Journées de la biodiversité dans le Vallon de Nant (Bex, Alpes vaudoises). undefined.Walter, F., Burtin, A., McArdell, B.W., Hovius, N., Weder, B., Turowski, J.M., 2017. Testing seismic amplitude source location for fast debris-flow detection at Illgraben, Switzerland. Natural Hazards and Earth System Sciences 17, 939–955. https://doi.org/10.5194/nhess-17-939-2017Welch, P., 1967. The use of fast Fourier transform for the estimation of power spectra: A method based on time averaging over short, modified periodograms. IEEE Transactions on Audio and Electroacoustics 15, 70–73. https://doi.org/10.1109/TAU.1967.1161901Wheaton, J.M., Brasington, J., Darby, S.E., Sear, D.A., 2010. Accounting for uncertainty in DEMs from repeat topographic surveys: improved sediment budgets. Earth Surface Processes and Landforms 35, 136–156. https://doi.org/10.1002/esp.1886Wohl, E., 2013. Mountain Rivers Revisited. John Wiley & Sons.Wohl, E., 2006. Human impacts to mountain streams. Geomorphology, 37th Binghamton Geomorphology Sym-

posium 79, 217–248. https://doi.org/10.1016/j.geomorph.2006.06.020Wolman, M.G., 1954. A method of sampling coarse river-bed material. EOS, Transactions American Geophysical Union 35, 951–956.Wu, L., Liu, X., Ma, X., 2018. Research progress on the watershed sediment delivery ratio. International Journal of Environmental Studies 75, 565–579. https://doi.org/10.1080/00207233.2017.1392771Wyss, C.R., Rickenmann Dieter, Fritschi Bruno, Turowski Jens M., Weitbrecht Volker, Boes Robert M., 2016. Measuring Bed Load Transport Rates by Grain-Size Fraction Using the Swiss Plate Geophone Signal at the Erlenbach. Journal of Hydraulic Engineering 142, 04016003. https://doi.org/10.1061/(ASCE)HY.1943-7900.0001090Yager, E.M., Dietrich, W.E., Kirchner, J.W., McArdell, B.W., 2012. Prediction of sediment transport in step-pool channels. Water Resources Research 48. https://doi.org/10.1029/2011WR010829Zhan, Z., 2019. Distributed Acoustic Sensing Turns Fiber-Optic Cables into Sensitive Seismic Antennas. Seismological Research Letters 91, 1–15. https://doi.org/10.1785/0220190112